scientific reports

Check for updates

OPEN

Synergistic performance of a new bimetallic complex supported on magnetic nanoparticles for Sonogashira and C–N coupling reactions

Fatemeh Nasseri[1,2], Mohammad Ali Nasseri[2]✉, Mohamad Zaman Kassaee[1] & Issa Yavari[1]

This paper describes the synthesis of a novel Cu–Ni bimetallic system comprising of magnetic nanoparticles, as the core, and 4-amino-3,5-bis(pyridin-2-yl)-1,2,4-triazole (4-ABPT), as a conjugated bridge, between nickel and copper species. With low Cu and Ni loading (0.06 mol% Ni, 0.08 mol% Cu), the resulting Fe_3O_4@SiO_2@4-ABPT/Cu–Ni showed to be a highly efficient catalyst for the Sonogashira and C–N cross-coupling reactions. The developed catalyst was well characterized by FT-IR, XRD, EDX-mapping, FE-SEM, TEM, ICP, VSM, TGA/DTG/DTA, LSV, and XPS techniques. Fe_3O_4@SiO_2@4-ABPT/Cu–Ni nanocatalyst was compatible with a wide range of amines and aryl halides in the Sonogashira and C–N cross-coupling reactions and offered desired coupling products in high to excellent yields under palladium- and solvent-free conditions. Based on the XPS results, the 4-ABPT ligand can adjust electron transfer between Ni and Cu in Fe_3O_4@SiO_2@4-ABPT/Cu–Ni, promoting the formation and stabilization of Cu^+ and Ni^{3+} species. Electronic interactions and the synergistic effect between these metals increased the selectivity and activity of Fe_3O_4@SiO_2@4-ABPT/Cu–Ni catalyst in the Sonogashira and C–N cross-coupling reactions compared with its monometallic counterparts. Additionally, the magnetic properties of Fe_3O_4@SiO_2@4-ABPT/Cu–Ni facilitated its separation from the reaction mixture, promoting its reuse for several times with no significant loss in its catalytic activity or performance.

Carbon–carbon and carbon-heteroatom cross-coupling reactions, which traditionally apply palladium catalysts, are among the most significant chemical processes in organic synthesis[1–5]. A look at the development of these reactions indicates their applications in materials science, agrochemical compounds, electronic materials, and polymers area[6–8]. For almost two decades, they have significantly influenced drug discovery and medicinal chemistry[9–11].

Despite the considerable prospects of palladium catalysts in cross-coupling reactions, the high cost and possible toxicity of Pd have remained a scientific challenge, highlighting the need for developing and discovering alternative ways with an environmentally friendly and non-toxic catalytic system[12–14]. Numerous studies have reported the use of other transition metals, such as Ni[15,16], Cu[17,18], Fe[19,20], and Co[21,22] for more appropriate, cost-effective, and safe approaches for cross-coupling reactions, over the past decade. Considerable attention has been given to copper catalysis, owing to its good functional group tolerance, the low cost of the catalysts, and low toxicity[23,24]. Besides, copper plays an essential role in cross-coupling reactions. Its scope and function in the bond-formation processes of C–heteroatom and C–C bonds have considerably increased[11,25].

Copper is crucial for cross-coupling reactions, but it suffers from several drawbacks like low activity and a propensity for oxidative homo-coupling reactions[21,26]. The drawbacks can be optimized by the introduction of a second metal into a Cu monometallic sample as a Cu–M bimetallic catalytic system. As a result, the geometric and electronic properties of the sample can be modified[27,28]. The synergistic effect of both metals improves the efficiency and selectivity of the catalyst[11,29].

[1]Department of Chemistry, Tarbiat Modares University, P.O. Box 14155-175, Tehran, Iran. [2]Department of Chemistry, Faculty of Basic Sciences, University of Birjand, P.O. Box 97175-615, Birjand, Iran. ✉email: manaseri@birjand.ac.ir

Nickel is an ideal candidate as the second metal for the following reasons. Ni has a high bonding affinity with sufficient flexibility to generate multiple oxidation states[30,31]. Furthermore, metal-catalyzed cross-coupling processes show that nickel is as reactive as palladium[26].

Over the past 20 years, several attempts have been made to develop heterogenous Cu–Ni bimetallic catalysts for improved cross-coupling reactions. In 2008, Lipshutz et al. synthesized a heterogeneous bimetallic catalyst of copper and nickel oxide particles supported within charcoal (Ni/Cu@C). It was the first example of a mixed-metal, recyclable catalyst composed of Cu and Ni that could mediate both groups 10 and group 11 cross-couplings[32]. Varadwaj and co-workers, in 2013, studied an amine-functionalized montmorillonite-supported Cu, Ni catalyst for C–S coupling reactions. As a bimetallic catalytic system, the strong synergistic interaction of Cu and Ni increased the yield of C–S couplings[27]. Recently, Nasresfahani et al. reported Ni/Cu-MCM-41 as a reusable and efficient bimetallic catalyst for the Sonogashira cross-coupling reactions[33].

Filtration or centrifugation techniques can be utilized to recover the majority of these heterogeneous catalysts. However, these processes are time-consuming and contaminate the product as the catalyst particles are lost. This issue can be resolved by employing magnetic Fe_3O_4@SiO_2 nanoparticles as a heterogeneous recoverable solid support with a high surface area. Conventional magnets can be simply used to separate the magnetically immobilized catalyst from the reaction media.

The existence of organic ligands on the support surface can facilitate the anchoring of metal ions/metals via chelation[34,35]. The properties of metal-complexed ligands may also regulate the activity and selectivity of the catalyst[36,37]. In bimetallic complexes, bridging ligands can be crucial in metal–metal interactions[38–42]. According to the through-bond super-exchange formalism, bridging ligands with π-conjugated structures are favored for accelerating electron transfer[43]. One of the most popular chelating ligands, which can be used as a bridge between metallic centers, is 4-Amino-3,5-bis(pyridin-2-yl)-1,2,4-triazole (4-ABPT)[44].

In this work, 4-ABPT was utilized as a ligand with a large conjugated system to synthesize Fe_3O_4@SiO_2@4-ABPT, as a suitable support, for stabilizing bimetallic Cu–Ni nanoparticles. To the best of our knowledge, there are some π-conjugated bimetallic systems that were unsupported on reusable magnetic materials and used as the catalytic systems for chemical reactions [40,45,46], but Fe_3O_4@SiO_2@4-ABPT/Cu–Ni is the first example of a π-conjugated system between two metals supported on reusable magnetic materials (Fig. 1). The resultant Fe_3O_4@SiO_2@4-ABPT/Cu–Ni nanocatalyst had excellent catalytic activity for Sonogashira and C–N cross-coupling reactions under solvent-free conditions. The present Cu–Ni bimetallic system benefits from the cooperativity between conjugated 4-ABPT ligand and Cu/Ni centers. Moreover, the Fe_3O_4 magnetic core in Fe_3O_4@SiO_2@4-ABPT/Cu–Ni nanocatalyst provides appropriate reusability in the cross-coupling reactions.

Experimental section

Materials and methods

All chemicals were purchased from Merck Company with high purity. NMR spectra were recorded using a Bruker Avance DPX-250 (^{1}H-NMR at 250 MHz and ^{13}C–NMR at 62.5 MHz) spectrometer in the deuterated ($CDCl_3$ and DMSO-d_6) solvents and TMS as the internal standard. The purity of the products and the reaction progress were evaluated by thin layer chromatography (TLC) on silica-gel Polygram SILG/UV254 plates. Fourier transform infrared (FT-IR) spectra were recorded on a JASCO FT/IR 4600 spectrophotometer using a KBr pellet. Melting points were measured on an Electro thermal 9100 apparatus. The images of field-emission scanning electron microscopy (FE-SEM) were taken by a Tescan Mira3 microscope. Energy-dispersive X-ray (EDX) spectroscopy was performed using a scanning electron microscope (SEM, FEI Quanta 200) equipped with an EDX detector. The presence of the elements was confirmed using the point elemental mapping (TESCAN MIRA 3 LMU). Transmission electron microscopy (TEM) analysis was accomplished by a TEM microscope (Philips EM 208S) operating at 100 kV. Thermogravimetry and differential thermal analysis (TGA-DTA) were performed using a Q600 model from TA Company; the sample was heated from 25 to 1000 °C at the rate of 10 °C min^{-1} under a nitrogen atmosphere. Vibrating-sample magnetometer (VSM) analysis was performed by LBKFB model-magnetic Kashan kavir. X-ray diffraction (XRD) patterns were obtained by a Philips-PW 1730 X-ray diffractometer incorporating Cu Kα radiation (λ = 0.154 nm). X-ray photoelectron spectroscopy (XPS) analyses were implemented using a Thermo Scientific K-Alpha XPS system (Thermo Fisher Scientific, U.S.A). The XPS spectra were deconvoluted by using Gaussian–Lorentzian curves. Linear sweep voltammetry (LSV) (Electrochemical measurements) of the samples was assessed by a three-electrode system including carbon paste electrode modified (MCPE) with Fe_3O_4@SiO_2@4-ABPT/Cu, Fe_3O_4@SiO_2@4-ABPT/Ni, and Fe_3O_4@SiO_2@4-ABPT/Cu–Ni as working electrodes, saturated calomel electrode (SCE) as reference electrode and platinum wire as an auxiliary electrode (Azar Electrode Co, Iran), using Ivium galvanostat/potentiostat (CmpactStat, Switzerland). Finally, the Cu and Ni contents on the catalyst were analyzed by an inductively coupled plasma-optical emission spectrophotometer (ICP-OES, 730-ES, Varian Inc.).

Synthesis of magnetic iron oxide (Fe_3O_4) nanoparticles

The Fe_3O_4 nanoparticles were synthesized via chemical co-precipitation using chlorine salts of Fe^{3+} and Fe^{2+} ions with a molar ratio of 2:1 in the presence of an ammonia solution, followed by the hydrothermal treatment. Typically, a mixture of $FeCl_3{\cdot}6H_2O$ (1.76 g, 6.5 mmol) and $FeCl_2.4H_2O$ (0.65 g, 3.3 mmol) was dissolved in the deionized water (100 mL), and the solution was vigorously stirred for 1 h under an argon atmosphere. Afterward, NH_4OH (6 mL of 25%) was dropwise added to the reaction mixture. The mixture was heated for 1 h at 80 °C, and the cooled black magnetite solid was collected with an external magnet, washed with distilled water, and dried under vacuum at 50 °C for 24 h.

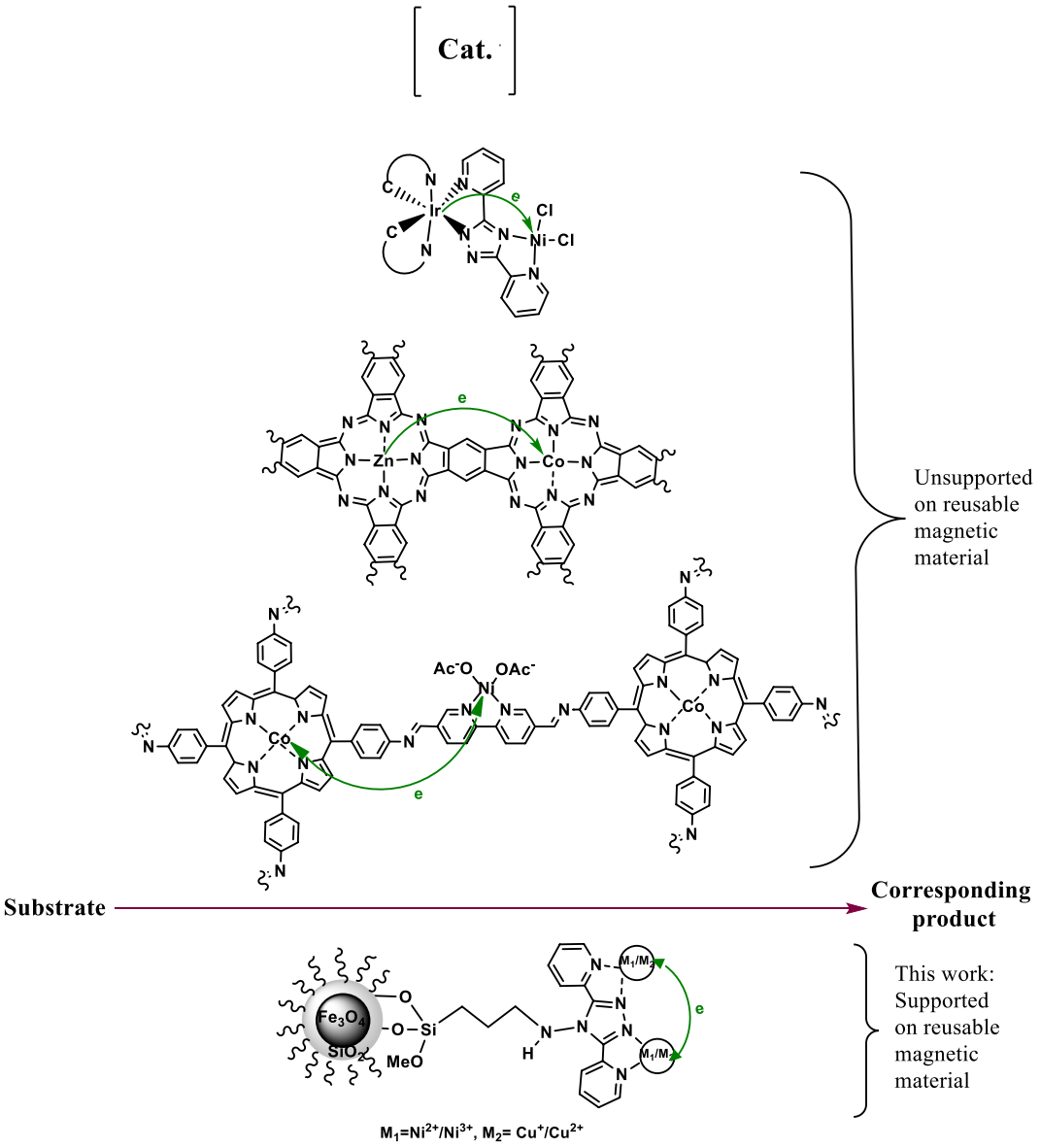

Figure 1. Importance of the π-conjugated bimetallic systems as the catalytic systems for chemical reactions.

Synthesis of silica-coated magnetic nanoparticles (Fe_3O_4@SiO_2)

Fe_3O_4 NPs (1 g) were dispersed in ethanol and distilled water (40:10 mL) under ultrasonication for 30 min. The pH was adjusted to 10 with an ammonia solution and then 1 mL tetraethyl orthosilicate (TEOS) was slowly dropped into the mixture over 10 min. After mechanical stirring for 12 h at 60 °C, the obtained Fe_3O_4@SiO_2 nanoparticles were separated by an external magnet, washed several times with ethanol, and dried under vacuum.

Synthesis of chloro-functionalized silica-coated magnetite nanoparticles (Fe_3O_4@SiO_2–Cl)

A mixture of Fe_3O_4@ SiO_2 (1.0 g) was dispersed in dry toluene (30 mL) by sonication for 45 min. Next, 3-chloropropyl trimethoxysilane (CPTMS, 1 mL) was dropwise added to the mixture and slowly heated to 105 °C. The mixture was stirred using a mechanical stirrer for 20 h under an argon atmosphere. After cooling to room temperature, the resulting chloro-functionalized Fe_3O_4@SiO_2 was collected using an external magnet, washed several times with CH_2Cl_2 and Et_2O, and dried under vacuum[47,48]. The Cl atom loading was 0.42 mmol per gram of catalyst based on the elemental analysis.

Synthesis of 4-Amino-3,5-bis(pyridin-2-yl)-1,2,4-triazole supported on Fe_3O_4@SiO_2 nanoparticles (Fe_3O_4@SiO_2@4-ABPT)

4-Amino-3,5-bis(pyridin-2-yl)-1,2,4-triazole (4-ABPT) was synthesized according to the literature procedure[49]. For the preparation of the supported 4-ABPT ligand, Fe_3O_4@SiO_2–Cl (0.3 g), 4-Amino-3,5-bis(pyridin-2-yl)-1,2,4-triazole (0.3 g, 1 mmol) and triethylamine (14 mL, 0.1 mol) were refluxed in dry toluene (40 mL) at 100 °C

for 24 h under argon atmosphere using a round-bottom flask fitted with a mechanical stirrer and condenser. Then, the obtained product (Fe_3O_4@SiO_2@4-ABPT) was separated with a permanent magnet, washed several times with toluene, and dried under vacuum.

Synthesis of Fe_3O_4@SiO_2@4-ABPT anchored Cu–Ni nanoparticles (Fe_3O_4@SiO_2@4-ABPT/Cu–Ni)

Finally, for the preparation of the copper-nickel bimetallic catalyst (Fe_3O_4@SiO_2@4-ABPT/Cu–Ni), 0.4 g of Fe_3O_4@SiO_2@4-ABPT was dispersed with $Cu(OAc)_2{\cdot}H_2O$ (0.02 g) and $Ni(OAc)_2.4H_2O$ (0.02 g) in ethanol (60 mL) to achieve 5 wt% of Cu and 5 wt% of Ni. The mixture was vigorously stirred for 12 h at 80 °C. Then, the cooled solid was collected with an external magnet and washed with EtOH (3 × 10 mL) .

General procedure for the Sonogashira cross-coupling reaction catalyzed by Fe_3O_4@SiO_2@4-ABPT/Cu–Ni

A mixture of phenylacetylene (1.5 mmol), aryl halide (1.0 mmol), NaO^{t}Bu (1.0 mmol), and Fe_3O_4@SiO_2@4-ABPT/Cu–Ni catalyst (0.01 g, 0.06 mol% Ni, 0.08 mol% Cu) was stirred at 120 °C under solvent-free conditions. TLC was utilized to monitor the progress of the reaction. After completion of the reaction, the reaction mixture was diluted with EtOAc (5 mL). Using an external magnet, Fe_3O_4@SiO_2@4-ABPT/Cu–Ni was separated as the catalyst and washed with EtOAc (2 × 10 mL) and EtOH (2 × 10 mL), dried under vacuum, and reused. Pure products were obtained by column chromatography (silica gel) using a 4:1 volume ratio of *n*-hexane: EtOAc as eluent.

General procedure for C–N cross-coupling reaction catalyzed by Fe_3O_4@SiO_2@4-ABPT/Cu–Ni

A mixture of aryl halide (or phenylboronic acid, 1.0 mmol), *N*-heterocyclic compound (1.3 mmol), NaO^{t}Bu (1.0 mmol), and Fe_3O_4@SiO_2@4-ABPT/Cu–Ni catalyst (0.01 g, 0.06 mol% Ni, 0.08 mol% Cu) was stirred at 120 °C under solvent-free conditions for the desired reaction time under TLC monitoring. Further, the reaction mixture was extracted with ethyl acetate (5 mL). The catalyst was separated with an external magnet, washed with EtOAc (2 × 10 mL) and EtOH (2 × 10 mL), and dried in vacuum. The pure coupling product was obtained by column chromatography (silica gel) using a 10:2 volume ratio of *n*-hexane: EtOAc as eluent.

Results and discussion

Figure 2 illustrates the approach used to prepare a Cu–Ni bimetallic catalyst (Fe_3O_4@SiO_2@4-ABPT/Cu–Ni). Initially, Fe_3O_4 NPs were synthesized through the chemical co-precipitation method, followed by silica coating by TEOS. Then, Fe_3O_4@SiO_2 was functionalized through reacting with 3-chloropropyl trimethoxysilane and subsequent treatment with 4-Amino-3, 5-bis(pyridin-2-yl)-1,2,4-triazole to produce Fe_3O_4@SiO_2@4-ABPT. Finally, Cu–Ni nanoparticles were immobilized onto Fe_3O_4@SiO_2@4-ABPT by adding $Cu(OAc)_2{\cdot}H_2O$ and $Ni(OAc)_2{\cdot}4H_2O$ precursors. The formation of the bimetallic system was verified using FT-IR spectroscopy, XRD, VSM, TGA, FE-SEM, EDX-mapping, TEM, XPS, and ICP techniques.

FT-IR spectra of Fe_3O_4, Fe_3O_4@SiO_2, Fe_3O_4@SiO_2@CPTMS, Fe_3O_4@SiO_2@4-ABPT, and Fe_3O_4@SiO_2@4-ABPT/Cu–Ni are depicted in Fig. 3. Curve **a** exhibits a strong absorption band at around 591 cm^{-1} which can be attributed to the Fe – O stretching vibrations in Fe_3O_4[50]. A broad high-intensity band near 1100 cm^{-1} in curve **b** can be ascribed to the Si–O-Si asymmetric stretching vibrations, while the weaker band at 800 cm^{-1} shows the symmetric stretching vibration of the Si–O–Si[51,52]. These results indicate that the silica layer is well formed around the magnetic core. Curve **c** exhibits the anchor of CPTMS onto the surface of Fe_3O_4@SiO_2 NPs by C–H stretching vibrations that appeared at ~ 2928 cm^{-1}[53,54]. Curve **d** demonstrates a peak at ~ 1652 cm^{-1} due to the stretching vibration of C═N in the pyridine ring. Also, the peak at about 1531 cm^{-1} can be ascribed to the N–H bending vibration. Furthermore, the IR spectrum illustrates two bands near 1468 and 1600 cm^{-1} corresponding to the aromatic rings. These vibrational bands suggest that the surface of Fe_3O_4@SiO_2 nanoparticles is successfully modified with the 4-ABPT ligand. Curve **e** shows a slight shift and variation in the amplitude of the N–H (a shift from 1531 to 1526 cm^{-1}) and C=N (a shift from1652 to 1640 cm^{-1}) bands of triazole, which can verify the coordination between the metals and the nitrogen atoms of Fe_3O_4@SiO_2@4-ABPT/Cu–Ni structure.

Figure 4 shows the XRD patterns of Fe_3O_4, Fe_3O_4@SiO_2, and Fe_3O_4@SiO_2@4-ABPT/Cu–Ni nanoparticles. The XRD pattern of Fe_3O_4, shows six main characteristic peaks at 2 θ = 30.31°, 35.91°, 43.87°, 54.01°, 57.66°, and 63.57°, corresponding to (220), (311), (400), (422), (511), and (440) planes, respectively (Fig. 4a). These reflections firmly verified the crystal structure of Fe_3O_4 consistent with that reported in the literature (JCPDS card no. 19-629)[55,56]. The same sets of characteristic peaks were also observed in the case of Fe_3O_4@SiO_2 NPs, suggesting the presence of the crystalline Fe_3O_4 NPs in their structures (Fig. 4b). Due to the amorphous structure of silica-coated on the Fe_3O_4 NPs, the SiO_2 peak was observed at 2θ = 15–25° in the XRD patterns of Fe_3O_4@SiO_2[57]. The presence of peaks corresponding to the Fe_3O_4 structure, as well as the amorphous silica peak, in the XRD pattern of Fe_3O_4@SiO_2@4-ABPT/Cu–Ni (Fig. 4c) indicates that the surface modification of the Fe_3O_4 NPs caused no change in their stability and crystalline structure. Moreover, a noticeable reduction can be seen in the intensity of the peaks of Fe_3O_4@SiO_2@4-ABPT/Cu–Ni (Fig. 4c) due to the coating of nanoparticles by 4-ABPT.

The magnetic properties of Fe_3O_4, Fe_3O_4@SiO_2, and Fe_3O_4@SiO_2@4-ABPT/Cu–Ni were investigated at room temperature using the vibrating sample magnetometer (VSM) technique (Fig. 5). The S-like magnetization curves with zero magnetic hysteresis loops suggest the superparamagnetic behavior of the samples. As illustrated in Fig. 5, the saturation magnetization (Ms) values of Fe_3O_4, Fe_3O_4@SiO_2, and Fe_3O_4@SiO_2@4-ABPT/Cu–Ni NPs are 73, 51.2, and 43.8 emu g^{-1}, respectively (Fig. 5a–c). High magnetization of the nanoparticles implies that they could be easily separated from the reaction media using a magnet. Furthermore, the decrease in the saturation magnetization of Fe_3O_4@SiO_2 and Fe_3O_4@SiO_2@4-ABPT/Cu–Ni can be due to the coated silica-shell or Cu/Ni-triazole complex on the surface of Fe_3O_4 (Fig. 5b,c).

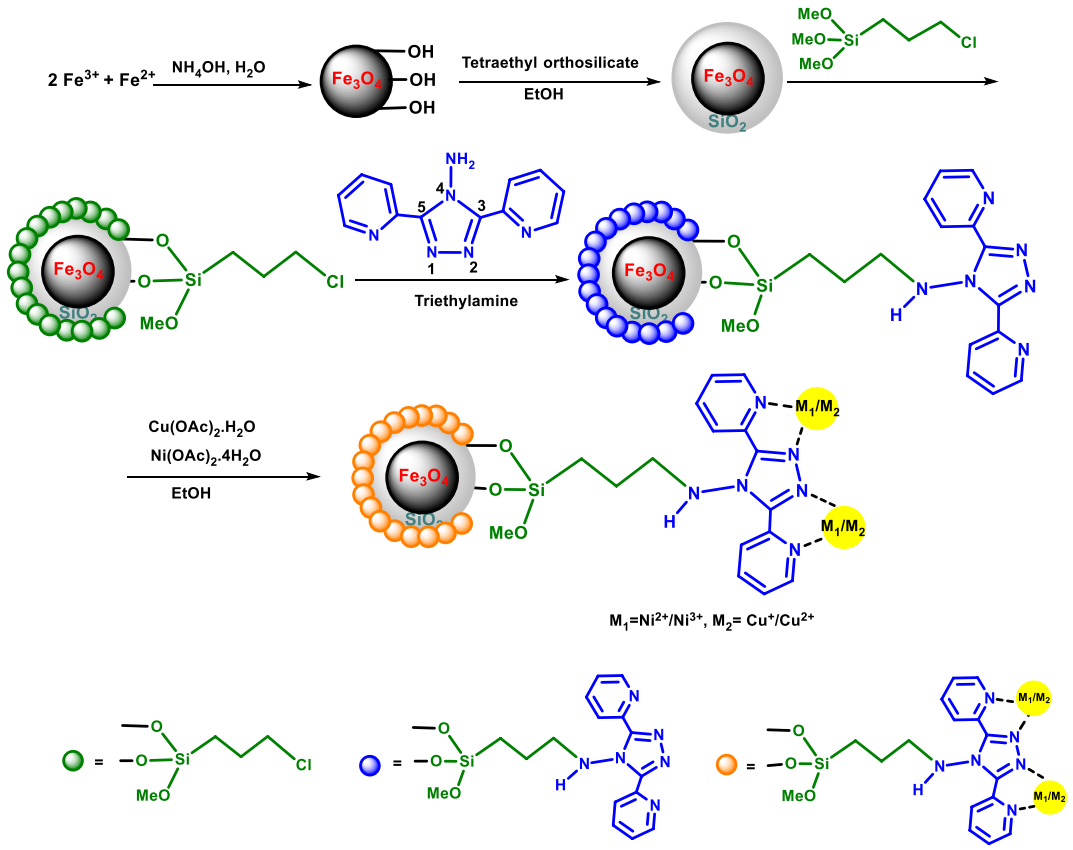

Figure 2. Preparation of Fe_3O_4@SiO_2@4-ABPT/Cu–Ni nanocatalyst.

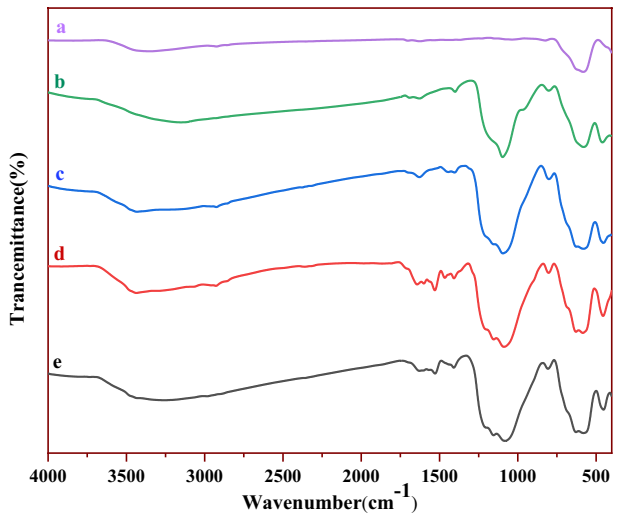

Figure 3. FT-IR spectra of (**a**) Fe_3O_4, (**b**) Fe_3O_4@SiO_2, (**c**) Fe_3O_4@SiO_2@CPTMS, (**d**) Fe_3O_4@SiO_2@4-ABPT, and (**e**) Fe_3O_4@SiO_2@4-ABPT/Cu–Ni.

Thermogravimetric analysis (TGA), differential thermogravimetric (DTG), and differential thermal analysis (DTA) techniques were utilized to investigate the thermal behavior of Fe_3O_4@SiO_2@4-ABPT/Cu–Ni and confirm the presence of functional groups on the surface of Fe_3O_4 nanoparticles. The TGA pattern shown in Fig. 6 exhibits three weight-loss steps in the catalyst. A slight weight loss of about 2% at temperatures below 100 °C can be assigned to the loss of the physically adsorbed water and residual organic solvents. Good thermal stability was seen at 100–250 °C, probably due to the strong chemical interactions between the SiO_2 coating layer, organic groups, and the Fe_3O_4 NPs. Other weight loss steps with an overall loss of about 3% at around 250–500 °C can be

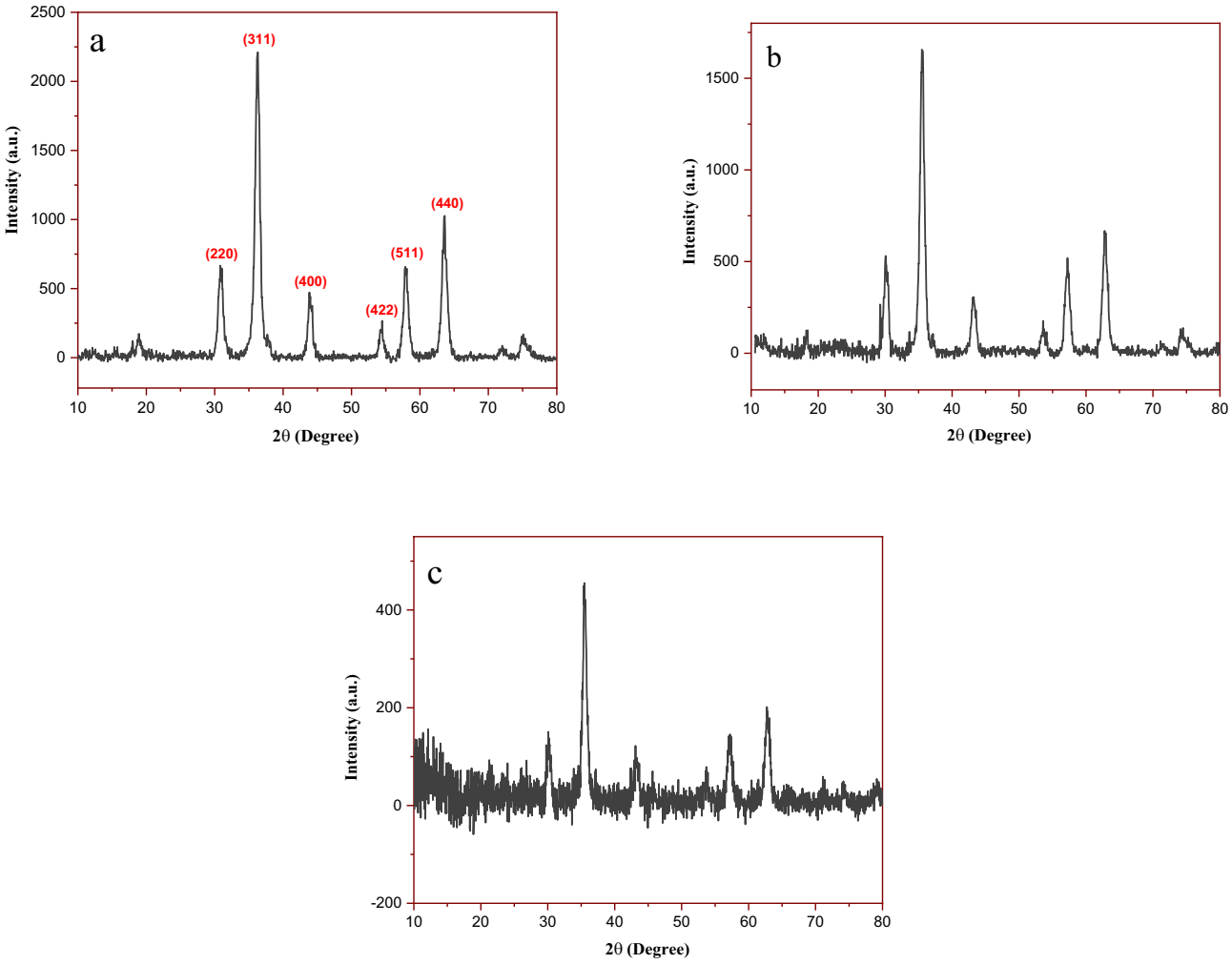

Figure 4. XRD patterns of (**a**) Fe_3O_4, (**b**) Fe_3O_4@SiO_2 and (**c**) Fe_3O_4@SiO_2@4-ABPT/Cu–Ni.

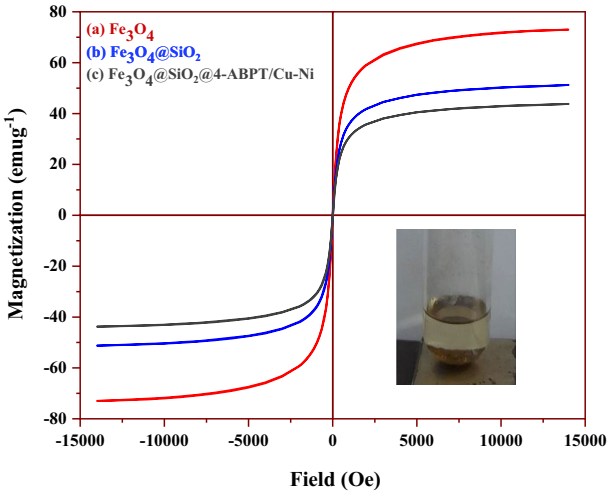

Figure 5. VSM analysis of (**a**) Fe_3O_4, (**b**) Fe_3O_4@SiO_2 and (**c**) Fe_3O_4@SiO_2@4-ABPT/Cu–Ni.

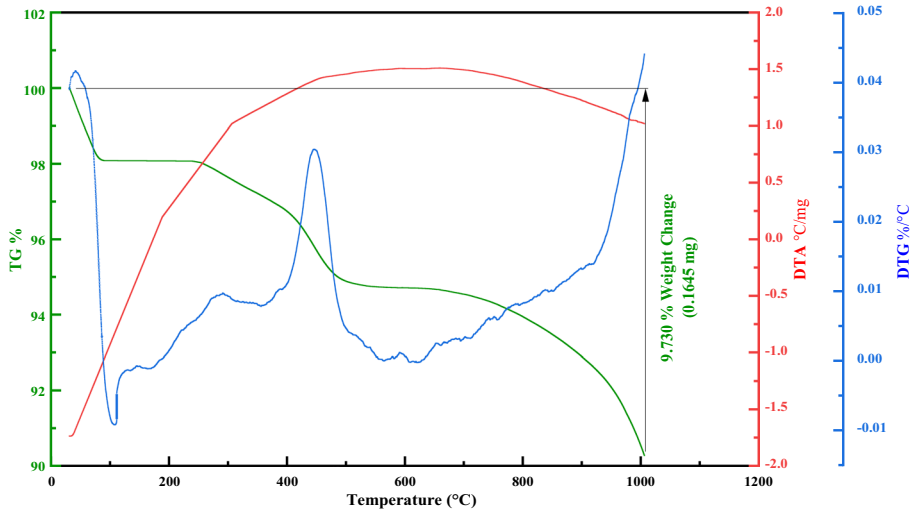

Figure 6. TG-DTG-DTA curves of Fe_3O_4@SiO_2@4-ABPT/Cu–Ni.

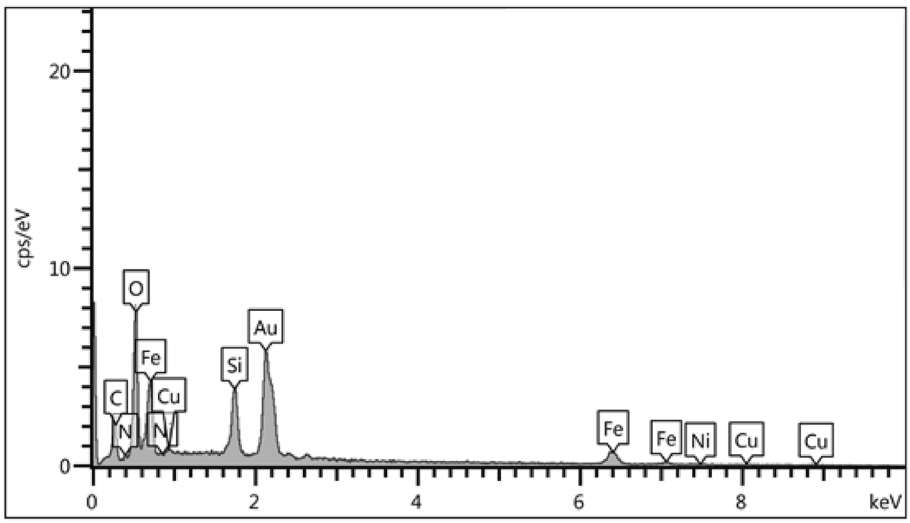

Figure 7. EDX analysis of Fe_3O_4@SiO_2@4-ABPT/Cu–Ni.

attributed to the thermal decomposition of supported organic moieties on the surface of Fe_3O_4@SiO_2 NPs. The complete decomposition of Fe_3O_4@SiO_2@4-ABPT/Cu–Ni, along with the possible phase transition of Fe_3O_4 to γ and α-Fe_2O_3, occurred at temperatures beyond 650 °C[58–60]. In general, the total weight loss of Fe_3O_4@SiO_2@4-ABPT/Cu–Ni was about 9.73%, suggesting little destruction and excellent heat resistance.

The chemical composition of Fe_3O_4@SiO_2@4-ABPT/Cu–Ni was determined by EDX analysis (Fig. 7). The results proved the existence of the expected elements in the structure of Fe_3O_4@SiO_2@4-ABPT/Cu–Ni, namely Si, C, N, O, Fe, Ni, and Cu.

To better show the elements on the surface of Fe_3O_4@SiO_2@4-ABPT/Cu–Ni, energy dispersive X-ray spectroscopy (EDS) mapping analysis was taken (Fig. 8). EDS elemental mapping of Fe_3O_4@SiO_2@4-ABPT/Cu–Ni confirmed the presence of all expected elements (Fe, Si, N, C, Ni, Cu, and O), and shows that all of them are evenly distributed over Fe_3O_4@SiO_2@4-ABPT/Cu–Ni.

FE-SEM and TEM images of Fe_3O_4@SiO_2@4-ABPT/Cu–Ni are shown in Fig. 9(a-d). In Fig. 9, a and b are FE-SEM images of Fe_3O_4@SiO_2@4-ABPT/Cu–Ni, and c and d are TEM images of Fe_3O_4@SiO_2@4-ABPT/Cu–Ni. All four images revealed the spherical morphology and uniform size of Fe_3O_4@SiO_2@4-ABPT/Cu–Ni NPs. Another interesting feature of the TEM images is that Fe_3O_4@SiO_2@4-ABPT/Cu–Ni NPs were highly dispersed. TEM images confirm the core–shell structure with an average size of 14 nm (Fig. 9c,d).

The Cu and Ni contents of the bimetallic catalyst (Fe_3O_4@SiO_2@4-ABPT/Cu–Ni) were calculated and quantified by an inductively coupled plasma analyzer (ICP). The exact Cu and Ni contents were estimated to be 0.08 and 0.06 mmol g^{-1}, respectively, suggesting the successful loading of Ni and Cu on the modified magnetic nanoparticles.

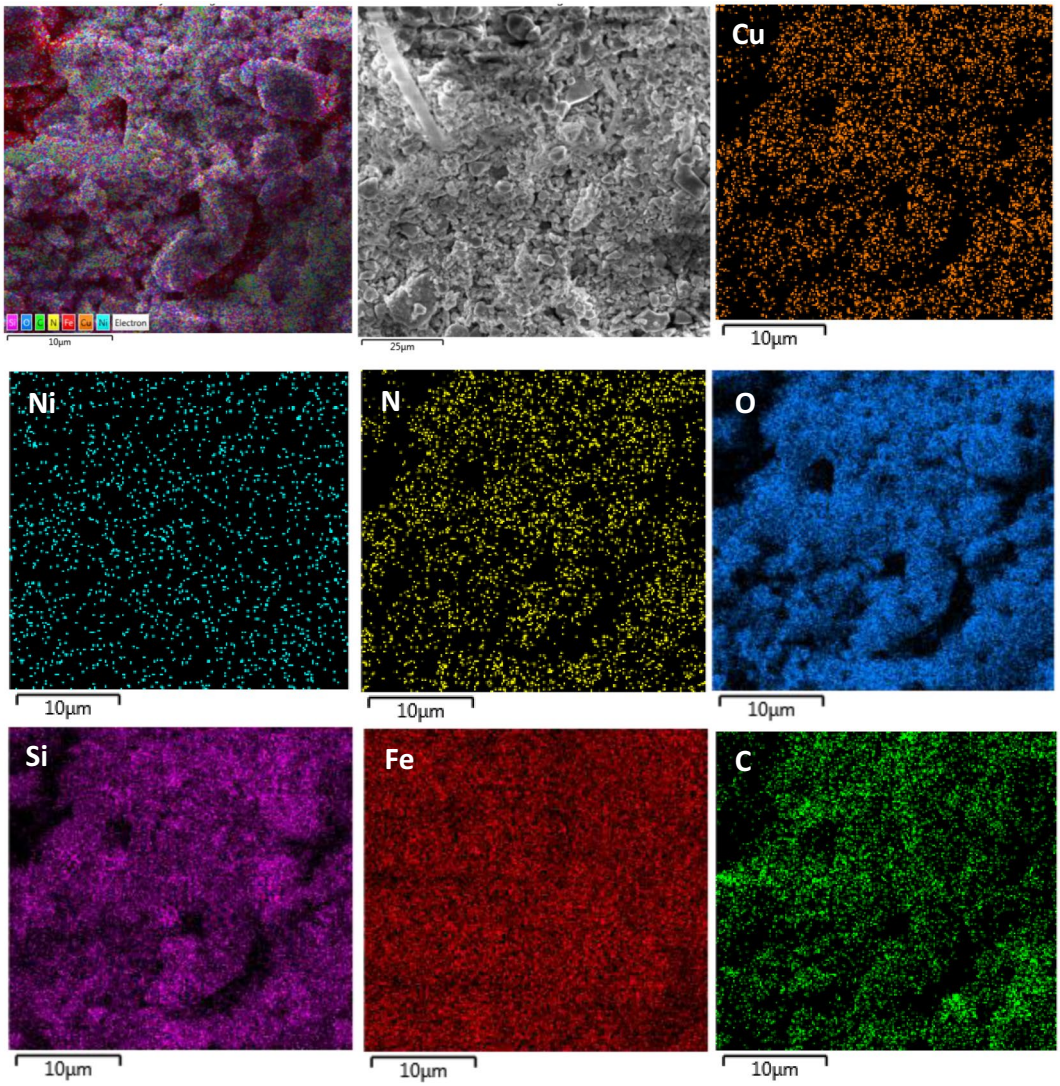

Figure 8. EDS elemental mappings of Fe_3O_4@SiO_2@4-ABPT/Cu–Ni.

To describe the chemical composition of Fe_3O_4@SiO_2@4-ABPT/Cu–Ni surface, a detailed XPS analysis was carried out (Fig. 10). The survey spectrum (Fig. 10a) proved the presence of carbon, nitrogen, silicon, iron, oxygen, nickel, and copper elements on the surface of Fe_3O_4@SiO_2@4-ABPT/Cu–Ni. The C 1s spectrum showed three main peaks (Fig. 10b). The first peak, located at approx. 284.8 eV, can be attributed to the C–C, C=C, and C–H aromatic bonds; the second peak at about 286.0 eV may be assigned to the C–N and C=N bonds; finally, the third peak at higher binding energy (located at approx. 288.7 eV) may be ascribed to the carbon atom of the C–O bond in the methoxy group (–OCH_3)[61,62]. The N 1s XPS spectrum was deconvoluted into four peaks centered at around 399.6, 401.1, 402.6, and 404.1 eV (Fig. 10c). The first peak can be attributed to the N atom in = N– structure[63,64]. The second one can be related to the pyrrole-like N[65,66]. The third peak at 402.6 may be attributed to triazole ring bonded amine N (–HN–C–)[67]. The last peak with weak intensity (404.1 eV) may be ascribed to the charging effect of triazole rings[68]. The deconvolution of the O 1s region showed two peaks (Fig. 10d). The first peak (located at approx. 530.1 eV) can be related to the lattice oxygen (O^{2-}) in the Fe_3O_4; the second peak at about 532.3 eV may be assigned to the oxygen of methoxy group (–OCH_3), O-Si, and adsorbed water[61,62,69]. Figure 10e shows the Cu 2*p* XPS spectra of the Fe_3O_4@SiO_2@4-ABPT/Cu–Ni nanocatalyst. The Cu $2p_{3/2}$ and Cu $2p_{1/2}$ binding energies are represented by two couples of peaks at 932.5 and 934.7 1 eV and 952.7 and 954.8 eV, reflecting the coexistence of Cu(I) and Cu(II) sites in Fe_3O_4@SiO_2@4-ABPT/Cu–Ni. In most cases, the spin–orbit splitting of the $2p_{3/2}$ and $2p_{1/2}$ peaks of Ni-containing compounds is large enough, so only the more intense $2p_{3/2}$ signal needs to be considered[27]. The spectrum of Ni $2p_{3/2}$ (Fig. 10f) exhibits binding energies at 855.9 and 856.7 eV corresponding to the nickel centers with + 2 and + 3 oxidation states, respectively. The accompanying satellite peaks of Ni $2p_{3/2}$ were observed at around 862 and 864.8 eV[70,71]. The relative amounts of Cu(I) and Ni(III) can be estimated by the integration of the peaks. As can be seen in Fig. 10e,f, the peak intensities of Cu(I) and Ni(III) are nearly equivalent to those of Cu(II) and Ni(II), respectively. The presence of conjugated ligand as a bridge in the bimetallic system helps to promote electron transfer between the Cu and Ni centers,

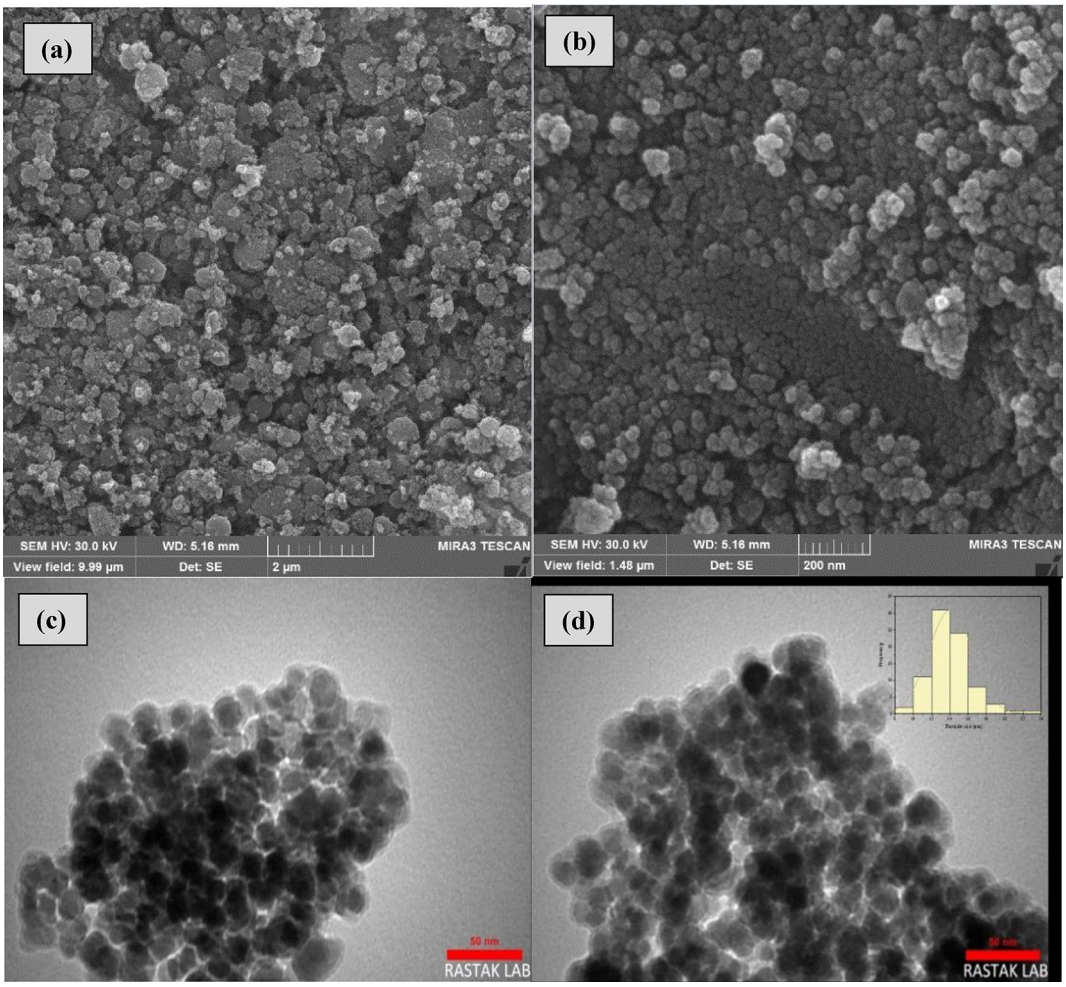

Figure 9. FE-SEM images of (**a** and **b**) Fe_3O_4@SiO_2@4-ABPT/Cu–Ni and TEM images of (**c** and **d**) Fe_3O_4@SiO_2@4-ABPT/Cu–Ni.

strengthening the synergistic effect and promoting the conversion of more Cu(II) and Ni(II) into active Cu(I) and Ni(III), respectively[46].

Optimization of reaction parameters

After the successful synthesis and characterization of Fe_3O_4@SiO_2@4-ABPT/Cu–Ni catalyst, its catalytic activity was probed in the Sonogashira C–C coupling reaction. The reaction parameters were optimized by the cross-coupling between aryl iodide and phenylacetylene as a simple model reaction. Several reaction factors, such as base type, temperature, solvent, and catalyst content were screened (Table 1). Based on Table 1, a range of polar and non-polar solvents was first investigated (Table 1, entries 1–12). However, an excellent yield of the desired product (85%) was obtained when the reaction was performed without solvent (Table 1, entry 13). Next, different amounts of Fe_3O_4@SiO_2@4-ABPT/Cu–Ni were examined in the model reaction (Table 1, entries 14–16). For this transformation, 0.01g of the catalyst containing 0.06 mol% Ni and 0.08 mol% Cu led to the best results (Table 1, entry 14). A further increase in the catalyst concentration substantially did not improve the yield (Table 1, entry 16). The effects of reaction temperature were also studied in the Sonogashira cross-coupling (Table 1, entries 17–20), where the best results were achieved at 120 °C (Table 1, entry 20). A lower yield was obtained when the reaction temperature was reduced (Table 1, entries 17–18). Finally, due to the significant role of bases in coupling reactions, various strong and weak bases were tested under identical reaction conditions (Table 1, entries 21–26). The best yield was obtained with NaO^{t}Bu (Table 1, entry 26). Accordingly, NaO^{t}Bu as the base, solvent-free conditions, 0.01 g of Fe_3O_4@SiO_2@4-ABPT/Cu–Ni (0.06 mol% Ni, 0.08 mol% Cu) as the amount of catalyst, and 120 °C as the optimum temperature was found to be the optimal conditions for Fe_3O_4@SiO_2@4-ABPT/Cu–Ni-catalyzed Sonogashira C–C coupling reactions (Table 1).

Under the optimized conditions, the scope of the Sonogashira cross-couplings was surveyed using various aryl halides and phenylacetylene in the presence of Fe_3O_4@SiO_2@4-ABPT/Cu–Ni nanocatalyst (Table 2). As shown in Table 2, three aryl iodides, bromides, and chlorides effectively reacted with phenylacetylene to produce the corresponding products at high to excellent yields (Table 2, 70–95%). It should be noted that the Sonogashira reaction was highly selective as no Glaser-type homo-coupling or other side-coupling product was observed.

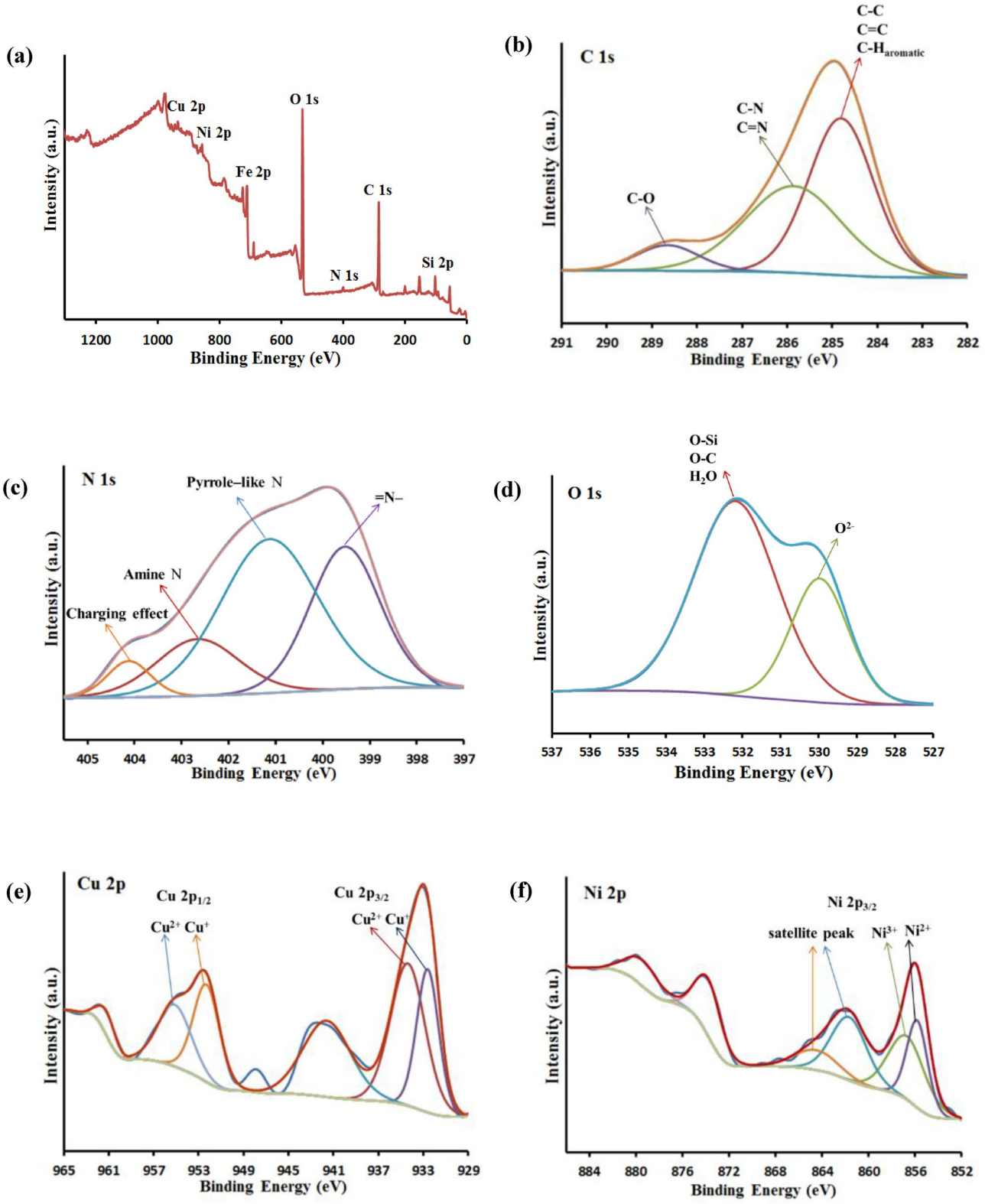

Figure 10. (**a**) XPS survey spectrum of Fe_3O_4@SiO_2@4-ABPT/Cu–Ni; high-resolution XPS spectra of (**b**) C 1s, (**c**) N 1s, (**d**) O 1s, (**e**) Cu 2p, and (**f**) Ni 2p of Fe_3O_4@SiO_2@4-ABPT/Cu–Ni.

Generally, aryl halides with electron-withdrawing functional groups such as $–NO_2$ and –CHO provided higher (produced better) efficiencies than those encompassing electron-donating substituents such as –OMe and –Me (Table 2, entries 2–4 versus 6–8). It means that a decline in the electron density of the aromatic ring accelerated

Entry[a]	Solvent	Catalyst (g)	Temp. (°C)	Base	Time (h)	Yield[b] (%)
1	H_2O	0.008	Reflux	NaOH	6	22
2	EtOH	0.008	Reflux	NaOH	4	80
3	$CHCl_3$	0.008	Reflux	NaOH	3.5	81
4	CH_2Cl_2	0.008	Reflux	NaOH	5.5	66
5	CH_3CN	0.008	Reflux	NaOH	4.5	70
6	THF	0.008	Reflux	NaOH	2	75
7	Toluene	0.008	Reflux	NaOH	3.5	31
8	DMSO	0.008	100	NaOH	2.5	76
9	MeOH	0.008	Reflux	NaOH	3	80
10	Dioxane	0.008	Reflux	NaOH	2.5	80
11	DMF	0.008	100	NaOH	3	74
12	EtOAc	0.008	Reflux	NaOH	5.5	60
13	none	0.008	100	NaOH	2	85
14	none	0.01	100	NaOH	1.5	86
15	none	0.005	100	NaOH	2	75
16	none	0.015	100	NaOH	1.5	87
17	none	0.01	70	NaOH	3.5	80
18	none	0.01	90	NaOH	2	82
19	none	0.01	140	NaOH	1	88
20	none	0.01	120	NaOH	1	88
21	none	0.01	120	KOH	1	83
22	none	0.01	120	NaOAc	3	75
23	none	0.01	120	K_2CO_3	4.5	75
24	none	0.01	120	K_3PO_4	3	80
25	none	0.01	120	Et_3N	5	82
26	none	0.01	120	NaO^{t}Bu	1	95

Table 1. Optimization of the reaction parameters for Sonogashira cross-coupling of phenylacetylene and iodobenzene catalyzed by Fe_3O_4@SiO_2@4-ABPT/Cu–Ni NPs. [a]Reaction conditions: phenylacetylene (1.5 mmol), iodobenzene (1.0 mmol), base (1 mmol), solvent (2 mL). [b]Isolated yield.

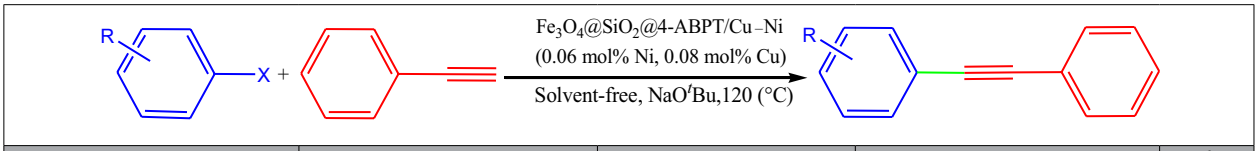

Entry[a]	R	X	Time (h)	Yield[b] (%)
1	H	I	1	95
2	4-Me	I	1.5	76
3	2-Me	I	2.5	73
4	4-OMe	I	3	75
5	4-CO_2H	I	1.5	87
6	4-NO_2	I	1	82
7	2-NO_2	I	1.5	80
8	4-COH	I	2	90
9	H	Br	1.5	90
10	4-NH_2	Br	4.5	74
11	4-CO_2H	Br	3	76
12	4-CN	Br	3.5	85
13	H	Cl	2.5	95
14	2-NH_2	Cl	4.5	75
15	3-NH_2	Cl	4	70
16	4-NH_2	Cl	4.5	78

Table 2. Sonogashira cross-coupling reaction of phenylacetylene with various aryl halides catalyzed by Fe_3O_4@SiO_2@4-ABPT/Cu–Ni NPs. [a]Reaction conditions: aryl halide (1.0 mmol), phenylacetylene (1.5 mmol), NaO^{t}Bu (1.0 mmol), solvent-free, catalyst (0.01 g, 0.06 mol% Ni, 0.08 mol% Cu), and 120 °C. [b]Isolated yield.

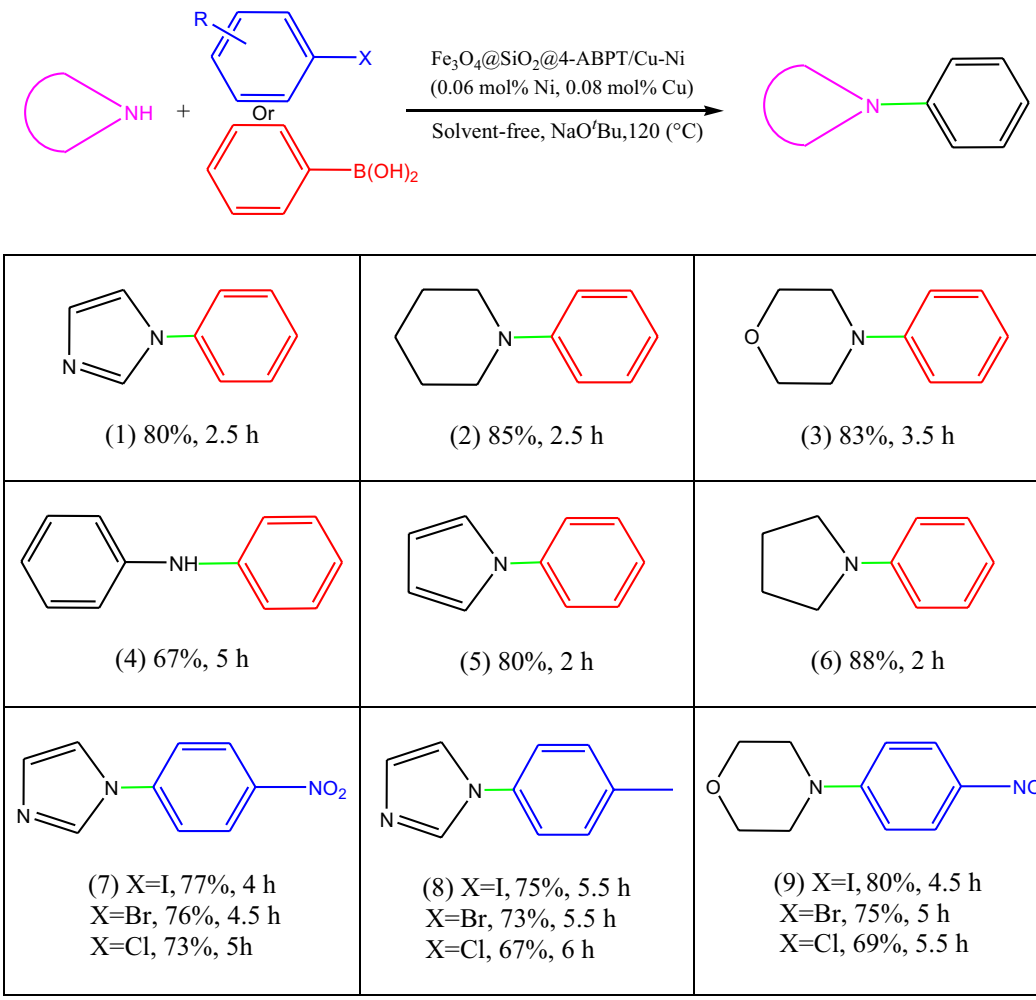

Table 3. C–N cross-coupling reaction of phenylboronic acid or aryl halides with *N*-heterocyclic compounds catalyzed by Fe_3O_4@SiO_2@4-ABPT/Cu–Ni NPs[a,b]. [a]Reaction conditions: aryl halide or phenylboronic acid (1 mmol), *N*-heterocyclic compound (1.3 mmol), NaO^tBu (1.0 mmol), solvent-free, catalyst (0.01 g, 0.06 mol% Ni, 0.08 mol% Cu), and 120 °C. [b]Isolated yield.

the halide elimination from the substrate in the oxidative-addition step of the Sonogashira cross-coupling reaction[72]. Moreover, the reactions of aryl iodides were slightly faster than their chloro and bromo analogs due to the lower C–I bond strength compared to C–Br and C–Cl bonds (C–Cl > C–Br > C–I)[73]. This order of reactivity, where aryl iodides are more reactive than aryl bromides and then aryl chlorides, is also in agreement with an oxidative addition/reductive elimination mechanism in which the rate-determining step is the breaking of the bond to the leaving group[4].

Due to the excellent results obtained from the Sonogashira cross-coupling reaction and the high performance of Fe_3O_4@SiO_2@4-ABPT/Cu–Ni nanocatalyst, under the optimum conditions obtained for the Sonogashira reaction, the carbon–nitrogen cross-couplings were also investigated. For this purpose, reactions were carried out at 120 °C in a solvent-free environment using Fe_3O_4@SiO_2@4-ABPT/Cu–Ni (0.01 g, 0.08 mol% Cu, 0.06 mol% Ni) and various aryl halides as well as phenylboronic acids with *N*-heterocyclic compounds. When compared to aryl halide derivatives, it was found that phenylboronic acid significantly influences the desired output product (Table 3, entries 1–6). The electron-withdrawing haloarenes react more quickly with imidazole than electron-donating haloarenes (Table 3, entries 7 vs. 8).

Control experiments

The high catalytic performance of Fe_3O_4@SiO_2@4-ABPT/Cu–Ni was elucidated by performing several control experiments, in which the catalytic activity of different species was studied for the Sonogashira cross-coupling model reaction under optimum conditions (Table 4). For a better comparison, the reaction time was considered constant. The corresponding results are summarized in Table 4. The results showed that the catalytic activity of Fe_3O_4@SiO_2@4-ABPT/Cu–Ni was unique compared to the other catalyst components alone: (1) Reaction in the absence of the catalyst showed no detectable efficiency (Table 4, entry 1), (2) Fe_3O_4 and Fe_3O_4@SiO_2 magnetic

Entry[a]	Catalyst	Yield[g] (%)
1	No catalyst	No reaction
2	Fe_3O_4	No reaction
3	Fe_3O_4@SiO_2	No reaction
4	Fe_3O_4@SiO_2@4-ABPT	No reaction
5[b]	Fe_3O_4@SiO_2@4-ABPT/Cu	65
6[c]	Fe_3O_4@SiO_2@4-ABPT/Ni	35
7[d]	$Cu(OAc)_2$. H_2O + $Ni(OAc)_2.4H_2O$	15
8[e]	Fe_3O_4@SiO_2@4-ABPT/Cu + Fe_3O_4@SiO_2@4-ABPT/Ni	75
9[f]	Fe_3O_4@SiO_2@4-ABPT/Cu–Ni	95

Table 4. Designed control experiments for our Sonogashira cross-coupling reaction. [a]Reaction conditions: phenylacetylene (1.5 mmol), iodobenzene (1.0 mmol), NaO^{t}Bu (1.0 mmol), solvent-free, Cat. (0.01 g), 120 °C, 1 h. [b](0.01 g, 0.08 mol% Cu). [c](0.01 g, 0.06 mol% Ni). [d,e](0.06 mol% Ni, 0.08 mol% Cu). [f](0.01 g, 0.06 mol% Ni, 0.08 mol% Cu). [g]Isolated yield.

nanoparticles did not display any catalytic effect (Table 4, entries 2,3), (3) As shown in Table 4, entry 4, no catalytic activity was observed for Fe_3O_4@SiO_2@4-ABPT NPs in the coupling model reaction, (4) By coordinating copper (Fe_3O_4@SiO_2@4-ABPT/Cu) or nickel (Fe_3O_4@SiO_2@4-ABPT/Ni) metals, the yield increased to 65% and 35%, respectively (Table 4, entries 5,6). These results manifested the catalytic efficiency of the copper and nickel metal centers for the Sonogashira cross-coupling reaction, (5) Without the 4-ABPT ligand, copper and nickel salts were used, but no remarkable product was produced (15%, Table 4, entry 7), indicating that the 4-ABPT ligand may be crucial for Fe_3O_4@SiO_2@4-ABPT catalytic system. (6) When a physical mixture of Fe_3O_4@SiO_2@4-ABPT/Cu and Fe_3O_4@SiO_2@4-ABPT/Ni was used, the yield was 75% (Table 4, entry 8). Significantly, the simultaneous presence of copper and nickel connected with 4-ABPT bridging ligand in the bimetallic nanocatalyst (Fe_3O_4@SiO_2@4-ABPT/Cu–Ni) provided a higher chemical yield (95%) compared to the monometallic counterparts, physical mixture of monometallic counterparts, and non-supported metal salts. The improved catalytic activity of this bimetallic system probably originated from a synergistic cooperative effect between conjugated 4-ABPT ligand, Ni, and Cu metal centers.

To better illustrate the merits of Fe_3O_4@SiO_2@4-ABPT/Cu–Ni for the C–C and C–N cross-coupling reactions, the present catalyst system was compared with several previously reported bimetallic catalysts. The results are shown in Table 5. The Fe_3O_4@SiO_2@4-ABPT/Cu–Ni catalyst showed several superiorities over other reports such as short reaction time, high efficiency, low catalyst loading, low metal toxicity, absence of toxic organic solvents, and simple catalyst recycling.

Mechanistic study

According to the results of control reactions, the simultaneous presence of nickel and copper centers connected with 4-ABPT has a synergistic effect, increasing catalyst efficiency significantly. The synergetic interactions between active metal sites may be enhanced by an organic linker that bridges different metal centers and plays a sensitive charge transfer role[80].

Entry	Reaction	Catalyst	Condition	Time (h)	Yield (%)
1[This work]	Sonogashira[a]	Fe_3O_4@SiO_2@4-ABPT/Cu–Ni (0.06 mol% Ni, 0.08 mol% Cu)	Solvent-free/120 °C/NaO^{t}Bu	1	95
2[74]		Pd–Cu–PA[b] (0.1 mol% Pd)	NMP/100 °C/Bu_3N	5	88
3[75]		PdCu@GQD@Fe_3O_4[c] (Pd 0.3 mol%, Cu 0.35 mol%)	DABCO/Toluene/50 °C	24	99
4[76]		Pd/Cu@MCC-PAMAM-PEI[d] (0.65 mol% Pd, 2.55 mol% Cu)	DMSO/80 °C/K_2CO_3/N_2 atmosphere	4	96
5[77]		Cu/Pd@Mod-PANI-3OH[e] (0.094 mol% Pd)	H_2O/80 °C /Et_3N	8	90
6[78]		Fe_3O_4@PEG/Cu–Co[f] (0.13 mol% Co, 0.37 mol% Cu)	H_2O/80 °C/base-free	3.5	95
7[This work]	C–N coupling[g]	Fe_3O_4@SiO_2@4-ABPT/Cu–Ni (0.06 mol% Ni, 0.08 mol% Cu)	Solvent-free/120 °C/NaO^{t}Bu	4.5	80
8[79]		Pd (I) dimer[h] (2 mol% Pd)	Toluene/40 °C/NaO^{t}Bu/AgOTf	4	71
9[78]		Fe_3O_4@PEG/Cu–Co (0.17 mol% Co, 0.47 mol% Cu)	H_2O/80 °C/base-free	7	75

Table 5. Comparison of catalyst efficiency of Fe_3O_4@SiO_2@4-ABPT/Cu–Ni with other methods described in the literature. [a]Sonogashira reaction of iodobenzene and phenylacetylene. [b]PA = Polyamide ligand. [c]GQD = Graphene quantum dot. [d]MCC-PAMAM-PEI = Polyethyleneimine end-capped microcrystalline cellulose-polyamidoamine dendrimer. [e]Mod-PANI-3OH = Modified polyaniline. [f]PEG = Polyethylene glycol. [g]C–N coupling reaction of 1-iodo-4-nitrobenzene and morpholine. [h]Phosphinoimidazole-derived Pd(I) complex.

In General, our observations and reported mechanisms suggest a plausible mechanism for the Fe_3O_4@SiO_2@4-ABPT/Cu–Ni-catalyzed Sonogashira cross-coupling reaction based on oxidative addition and reductive elimination steps[78,81,82]. It is impossible to certainly recognize which metal carries out the reaction via oxidative addition and reductive elimination [78]. However, a proposed mechanism on the basis of our results and previous reports is outlined in Fig. 11, in which the copper metal is suggested to perform the reaction. In the first step, electron transfer from Ni^{2+} through the 4-ABPT ligand led to the reduction of Cu^{2+} to Cu^{+}. Then, a π-complex is created between the acetylene groups and the metal centers of the catalyst. Cu^{+} activates phenylacetylene by generating transient copper acetylide intermediate B in the presence of NaO^{t}Bu. Oxidative addition of aryl halides to Cu^{+1} produces Cu^{+3}. Finally, a reductive elimination reaction forms the desired coupling product from the resulting intermediate C, and the catalyst returns to the cycle (Fig. 11a).

As shown in Fig. 11b , a similar mechanism can be proposed for the Fe_3O_4@SiO_2@4-ABPT/Cu–Ni-catalyzed C–N cross-coupling reaction. Initially, the nucleophilic attack of the amine group on the formed active Cu(I) species gives intermediate A. The proton is then taken away from the amine by NaO^{t}Bu, leading to the formation of intermediate B. After this, the oxidative addition of aryl halide close to intermediate B causes intermediate C, and the active centers of Cu(I) are oxidized to Cu(III). Ultimately, a reductive elimination stage resulted in the C–N coupling product and the regeneration of the bimetallic catalyst.

To explore the reaction mechanism more precisely and better investigate the synergistic effect between Ni and Cu species, some analysis was performed.

The electrochemical behavior of Fe_3O_4@SiO_2@4-ABPT/Cu, Fe_3O_4@SiO_2@4-ABPT/Ni, and Fe_3O_4@SiO_2@4-ABPT/Cu–Ni was studied by linear sweep voltammetry (LSV) technique in the potential range of − 2.0 to + 2.0 V (Fig. 12). The LSV voltammogram of Fe_3O_4@SiO_2@4-ABPT/Cu shows a weak peak at the A area corresponding to Cu(I) ⇌ Cu(II), indicating low electron transfer process (Fig. 12a). The LSV voltammogram of Fe_3O_4@SiO_2@4-ABPT/Ni demonstrates a weak peak at the B area, which is related to Ni(II) ⇌ Ni(III), indicating low electron transfer process (Fig. 12b). In the LSV voltammogram of Fe_3O_4@SiO_2@4-ABPT/Cu–Ni, both peaks at A and B areas, which correspond to Cu(I) ⇌ Cu(II) and Ni(II) ⇌ Ni(III) respectively, exhibit strong current. The peaks intensity of Fe_3O_4@SiO_2@4-ABPT/Cu–Ni is significantly increased compared to the peaks intensity of its monometallic counterparts (Fe_3O_4@SiO_2@4-ABPT/Cu and Fe_3O_4@SiO_2@4-ABPT/Ni), suggesting proper electron transfer due to synergistic effect between the copper and nickel metals in Fe_3O_4@SiO_2@4-ABPT/Cu–Ni.

Considering the case of the Sonogashira reaction, XPS analysis of the recovered catalyst was performed (Fig. 13). Figure 13a shows the high-resolution spectra of Cu 2p for recovered Fe_3O_4@SiO_2@4-ABPT/Cu–Ni nanocatalyst. The peak area ratio of Cu^{+}/Cu^{2+} was 0.8, while this ratio was 0.7 for the fresh catalyst. The increase in Cu^{+} production suggests that Cu^{+} might be the active center during the catalytic process. Noteworthy, the peak position of Cu^{+} at $2p_{1/2}$ was significantly shifted to lower binding energy (951 eV) compared with that of fresh catalyst (952.7 eV, Fig. 10e), indicating that the Ni atoms contribute to increasing the electronic density of Cu centers and facilitates the oxidative addition of haloarenes to Cu(I)[83,84]. Figure 13b shows the high-resolution XPS spectra of Ni 2p for used Fe_3O_4@SiO_2@4-ABPT/Cu–Ni. A slight positive shift can be seen to higher binding energy (857.5 eV) for Ni^{3+} relative to that of the unused catalyst (856.7, Fig. 10f), indicating that electron might

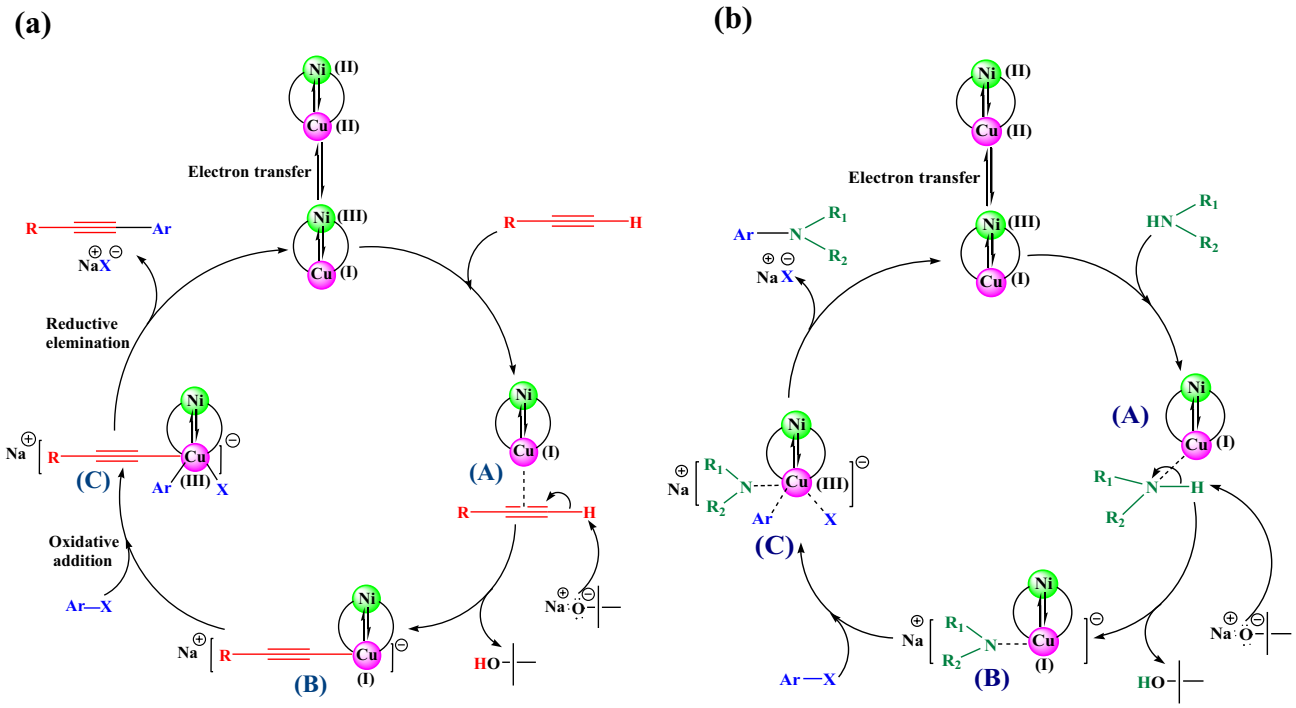

Figure 11. A plausible reaction mechanism for Fe_3O_4@SiO_2@4-ABPT/Cu–Ni-catalyzed (**a**) Sonogashira and (**b**) C–N cross-coupling reactions.

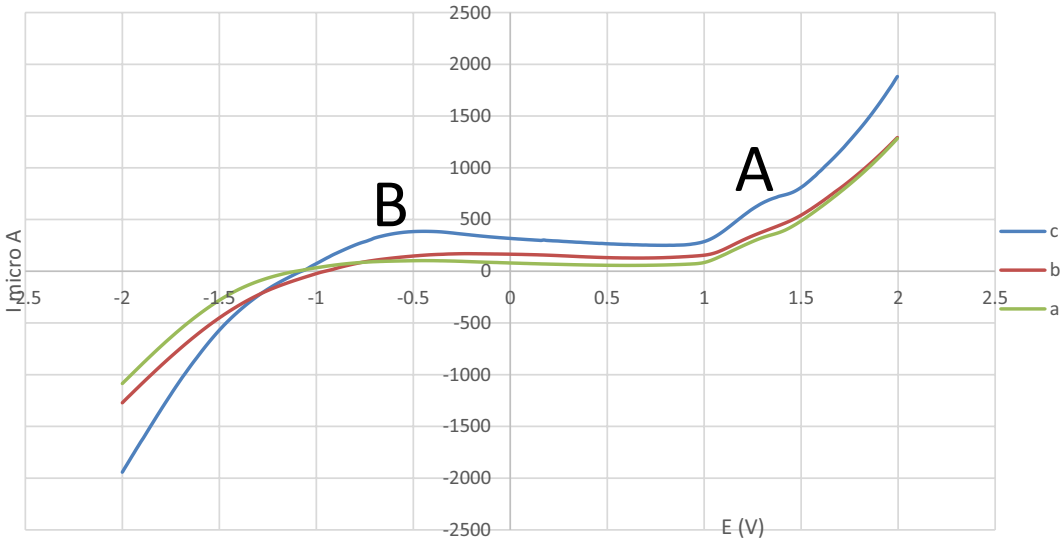

Figure 12. LSV voltammogram of (**a**) Fe_3O_4@SiO_2@4-ABPT/Cu, (**b**) Fe_3O_4@SiO_2@4-ABPT/Ni, and (**c**) Fe_3O_4@SiO_2@4-ABPT/Cu–Ni in 0.1 mol L^{-1} Britton–Robinson (BR) buffer solution (pH 7.0) with a scan rate of 100 mV s^{-1} at room temperature.

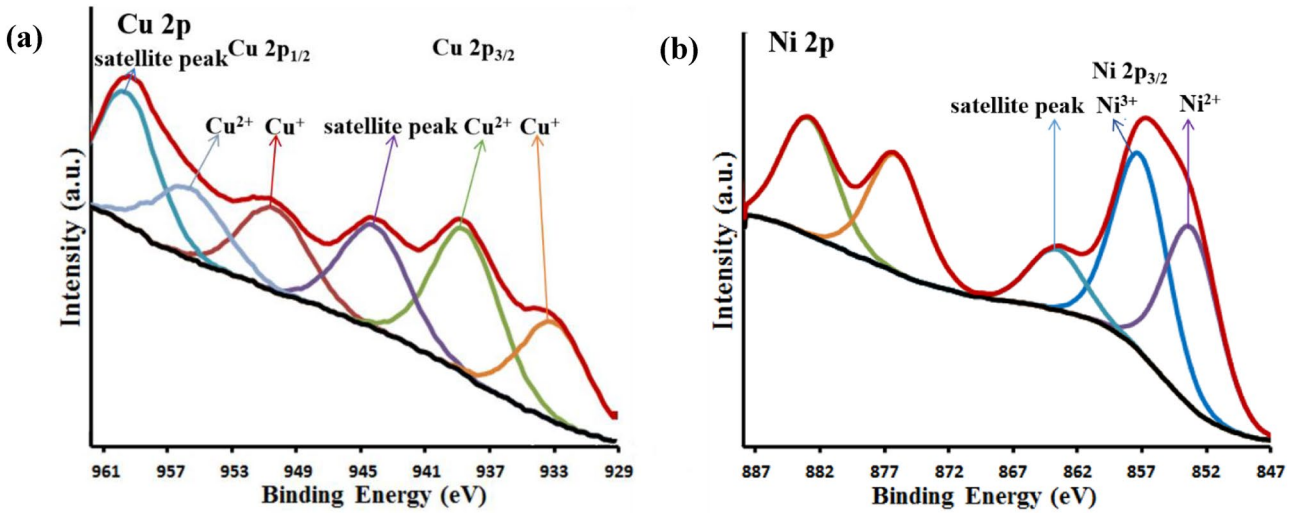

Figure 13. The high-resolution XPS spectra of (**a**) Cu 2p and (**b**) Ni 2p of recovered Fe_3O_4@SiO_2@4-ABPT/Cu–Ni.

transfer from Ni to Cu occurred due to the cooperation between Ni and Cu[85,86]. All these points helped to explain the existence of interactions between copper and nickel species.

Based on the results of the above analyses, the proposed mechanism and synergistic effect between copper and nickel metal centers can be verified.

Recoverability studies

Based on sustainable and green chemistry principles, catalyst reusability and stability are critical factors in evaluating the efficiency of a heterogeneous catalyst. In this way, we studied the recovery and recycling of Fe_3O_4@SiO_2@4-ABPT/Cu–Ni nanocatalyst in the model reaction of Sonogashira cross-coupling under optimal reaction conditions (Fig. 14). As shown in Fig. 14, Fe_3O_4@SiO_2@4-ABPT/Cu–Ni demonstrated a relatively consistent product yield after five successive runs with minimal efficiency loss. The efficiency reached 87% (a mere 8% decrease) after five runs, which is negligible.

FT-IR, TEM, and ICP analyses were used to characterize the recovered Fe_3O_4@SiO_2@4-ABPT/Cu–Ni nanocatalyst after the fifth run to determine its stability (Fig. 15a,b). The main structure of the nanocatalyst was preserved after successive recoveries and reuses, as shown by the FT-IR analysis of the recovered catalyst, which was almost identical to that of the fresh sample (Fig. 15a). The TEM image of the recovered Fe_3O_4@SiO_2@4-ABPT/Cu–Ni demonstrated no morphological changes after the 5th cycle (Fig. 15b). Based on ICP analysis, the amount

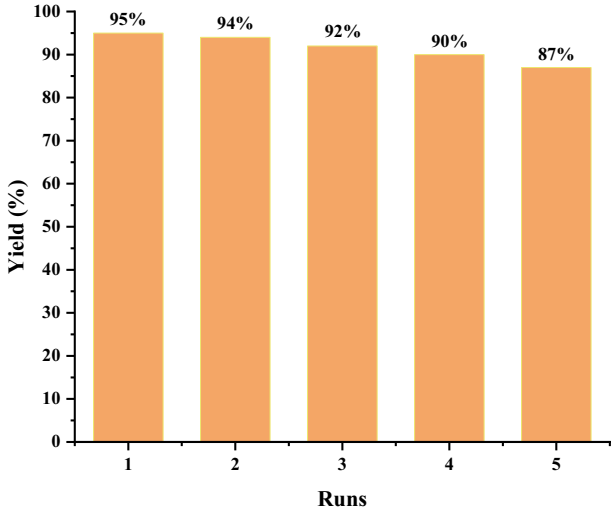

Figure 14. Recyclability of Fe_3O_4@SiO_2@4-ABPT/Cu–Ni NPs in the Sonogashira reaction of iodobenzene (1 mmol) with phenylacetylene (1.5 mmol) in the presence of Fe_3O_4@SiO_2@4-ABPT/Cu–Ni (0.01 g, 0.06 mol% Ni, 0.08 mol% Cu), and NaO^{t}Bu (1.0 mmol) at 120 °C for 1 h under solvent-free conditions.

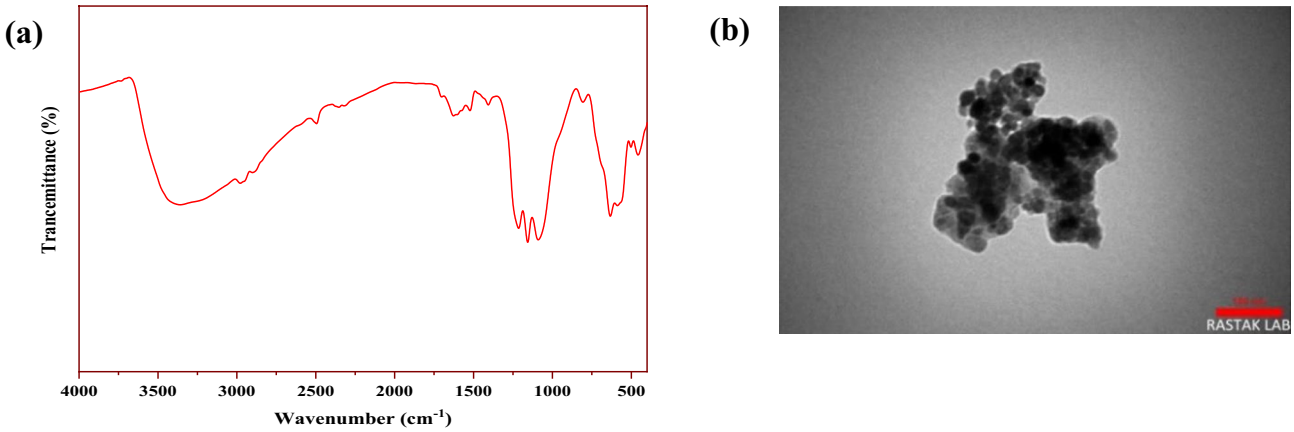

Figure 15. FT-IR spectrum (**a**) and TEM image (**b**) of the reused Fe_3O_4@SiO_2@4-ABPT/Cu–Ni nanocatalyst after the 5th run.

of copper and nickel was 0.073 and 0.051 mmol g^{-1}, respectively, suggesting negligible copper and nickel leaching (the Cu and Ni contents of the fresh catalyst were 0.08 and 0.06 mmol g^{-1}, respectively).

Conclusion

Briefly, this research reports the synthesis of a new magnetically recyclable Cu–Ni bimetallic system containing π-conjugated 4-ABPT bridging ligand (Fe_3O_4@SiO_2@4-ABPT/Cu–Ni). Fe_3O_4@SiO_2@4-ABPT/Cu–Ni was then characterized by FT-IR, XRD, EDX-mapping, LSV, FE-SEM, TEM, TGA, ICP, VSM, and XPS analyses. The developed nanocatalyst served well in the selective C–N and Sonogashira cross-coupling reactions under Pd- and solvent-free conditions. Fe_3O_4@SiO_2@4-ABPT/Cu–Ni nanocatalyst displayed high catalytic performance for various substrates despite its low copper and nickel contents (0.06 mol% Ni, 0.08 mol% Cu). By running the C–N and Sonogashira cross-coupling reactions with monometallic counterparts (Fe_3O_4@SiO_2@4-ABPT/Cu and Fe_3O_4@SiO_2@4-ABPT/Ni), the synergic effect of Fe_3O_4@SiO_2@4-ABPT/Cu–Ni as a conjugated bimetallic system can be revealed. According to the XPS results for the peak intensities of the Cu and Ni species in Fe_3O_4@SiO_2@4-ABPT/Cu–Ni, an electron can be transferred from Ni(II) to Cu(II) through the conjugated 4-ABPT ligand to form the active Cu(I) species. The copper center of Fe_3O_4@SiO_2@4-ABPT/Cu–Ni is suggested to carry out the cross-coupling processes via an oxidative addition/reductive elimination pathway. The catalytic synergy between ligand, Ni, and Cu led to high activity and selectivity of Fe_3O_4@SiO_2@4-ABPT/Cu–Ni as a catalyst in the cross-coupling transformations. Furthermore, the magnetic properties of Fe_3O_4@SiO_2@4-ABPT/Cu–Ni nanoparticles promoted its separation and reuse while streamlining the work-up process. FT-IR and TEM analyses of the recovered Fe_3O_4@SiO_2@4-ABPT/Cu–Ni demonstrated its stability after the fifth cycle. These analyses revealed that its proposed structure and morphology were nearly identical to those of the fresh one. Hence,

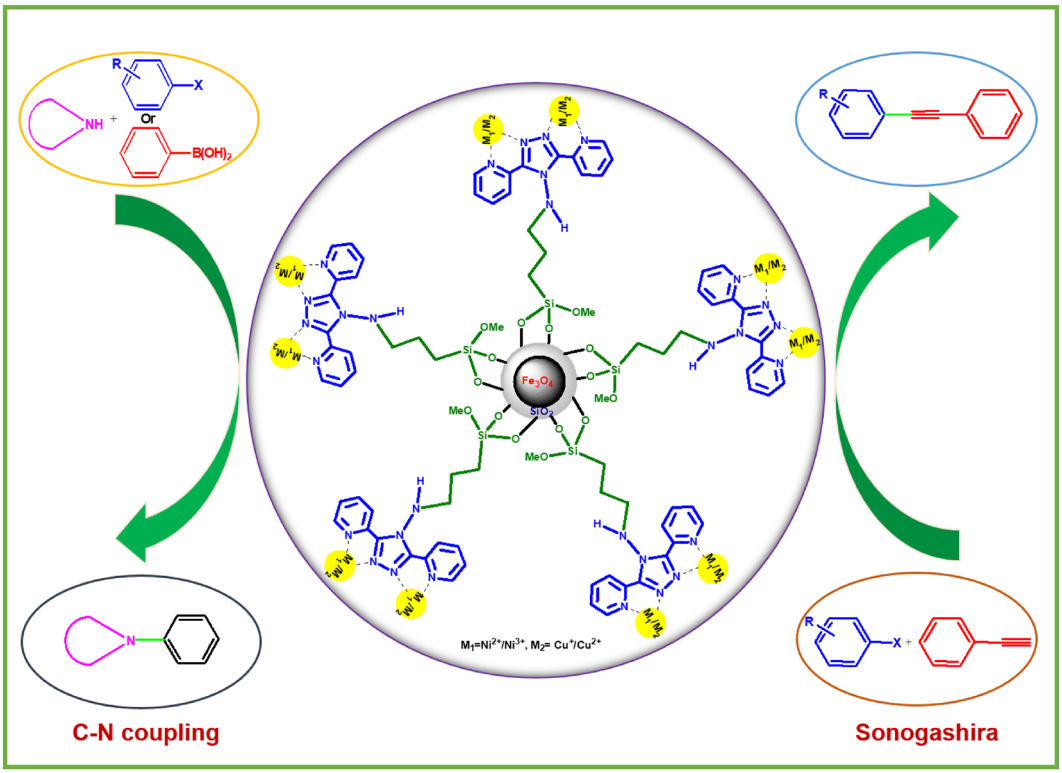

Figure 16. Graphical abstract.

Fe_3O_4@SiO_2@4-ABPT/Cu–Ni nanomaterial can be a promising catalyst for the industrial manufacturing of arylamine and biphenylacetylene derivatives (Fig. 16).

Data availability

All data generated or analyzed during this study are included in this published article (and its Supplementary Information files).

Received: 10 April 2023; Accepted: 4 October 2023
Published online: 24 October 2023

References

1. Huang, L., Ji, T. & Rueping, M. Remote nickel-catalyzed cross-coupling arylation via proton-coupled electron transfer-enabled C–C bond cleavage. *J. Am. Chem. Soc.* **142**, 3532–3539. https://doi.org/10.1021/jacs.9b12490 (2020).
2. Reimann, C. E., Kim, K. E., Rand, A. W., Moghadam, F. A. & Stoltz, B. M. What is a cross-coupling? An argument for a universal definition. *Tetrahedron* **130**, 133176. https://doi.org/10.1016/j.tet.2022.133176 (2022).
3. Mohjer, F., Mofatehnia, P., Rangraz, Y. & Heravi, M. M. Pd-free, Sonogashira cross-coupling reaction. An update. *J. Organomet. Chem.* **936**, 121712 (2021).
4. Rajalakshmi, C. *et al.* Theoretical investigation into the mechanism of copper-catalyzed Sonogashira coupling using trans-1, 2-diamino cyclohexane ligand. *Polyhedron* **193**, 114869 (2021).
5. Dong, Z. *et al.* Palladium immobilized on a polyimide covalent organic framework: An efficient and recyclable heterogeneous catalyst for the Suzuki-Miyaura coupling reaction and nitroarene reduction in water. *Catal. Lett.* **152**, 299–306 (2022).
6. Ranu, B. C., Adak, L., Mukherjee, N. & Ghosh, T. Benign metal catalyzed carbon-carbon and carbon-heteroatom bond formation. *Synlett.* **34**, 601–621 (2022).
7. Yang, Q. *et al.* Mizoroki-Heck cross-coupling of bromobenzenes with styrenes: Another example of Pd-catalyzed cross-coupling with potential safety hazards. *Org. Process Res. Dev.* **23**, 2148–2156. https://doi.org/10.1021/acs.oprd.9b00126 (2019).
8. Hassan, Z., Spuling, E., Knoll, D. M. & Bräse, S. Regioselective functionalization of [2.2]paracyclophanes: Recent synthetic progress and perspectives. *Angew. Chem. Int. Ed.* **59**, 2156–2170. https://doi.org/10.1002/anie.201904863 (2020).
9. Rayadurgam, J., Sana, S., Sasikumar, M. & Gu, Q. Palladium catalyzed C–C and C–N bond forming reactions: An update on the synthesis of pharmaceuticals from 2015–2020. *Org. Chem. Front.* **8**, 384–414 (2021).
10. Buskes, M. J. & Blanco, M.-J. Impact of cross-coupling reactions in drug discovery and development. *Molecules* **25**, 3493 (2020).
11. Kishore, D. R., Sreenivasulu, C., Dapkekar, A. B. & Satyanarayana, G. Recent applications on dual-catalysis for C–C and C–X cross-coupling reactions. *SynOpen* **6**, 179–194 (2022).
12. Niakan, M. & Masteri-Farahani, M. Pd–Ni bimetallic catalyst supported on dendrimer-functionalized magnetic graphene oxide for efficient catalytic Suzuki-Miyaura coupling reaction. *Tetrahedron* **108**, 132655 (2022).
13. Jia, X. *et al.* Low-crystalline PdCu alloy on large-area ultrathin 2D carbon nitride nanosheets for efficient photocatalytic Suzuki coupling. *Appl. Catal. B Environ.* **300**, 120756. https://doi.org/10.1016/j.apcatb.2021.120756 (2022).
14. Dong, Z. *et al.* Palladium supported on urea-containing porous organic polymers as heterogeneous catalysts for C–C cross coupling reactions and reduction of nitroarenes. *J. Saudi Chem. Soc.* **25**, 101317 (2021).

15. Kranthikumar, R. Recent advances in C(sp3)–C(sp3) cross-coupling chemistry: A dominant performance of nickel catalysts. *Organometallics* **41**, 667–679. https://doi.org/10.1021/acs.organomet.2c00032 (2022).
16. Karkon, E. G. & Mostafavi, H. A novel Fe_3O_4@TCH@ Ni(II) nanoparticle: An efficient magnetically retrievable nanocatalyst for C–C and C–heteroatom bond formation reaction. *Appl. Organomet. Chem.* **36**, e6824 (2022).
17. Yang, Q., Zhao, Y. & Ma, D. Cu-mediated Ullmann-type cross-coupling and industrial applications in route design, process development, and scale-up of pharmaceutical and agrochemical processes. *Org. Process Res. Dev.* **26**, 1690–1750. https://doi.org/10.1021/acs.oprd.2c00050 (2022).
18. Wang, F.-L. *et al.* Mechanism-based ligand design for copper-catalysed enantioconvergent C(sp3)–C(sp) cross-coupling of tertiary electrophiles with alkynes. *Nat. Chem.* **14**, 949–957 (2022).
19. Zhang, J., Wang, S., Zhang, Y. & Feng, Z. Iron-catalyzed cross-coupling reactions for the construction of carbon-heteroatom bonds. *Asian J. Org. Chem.* **9**, 1519–1531 (2020).
20. Ai, H. J. *et al.* Iron-catalyzed alkoxycarbonylation of alkyl bromides *via* a two-electron transfer process. *Angew. Chem. Int. Ed.* **61**, e202211939 (2022).
21. Khorsandi, Z., Hajipour, A. R., Sarfjoo, M. R. & Varma, R. S. A Pd/Cu-Free magnetic cobalt catalyst for C–N cross coupling reactions: Synthesis of abemaciclib and fedratinib. *Green Chem.* **23**, 5222–5229 (2021).
22. Khorsandi, Z., Keshavarzipour, F., Varma, R. S., Hajipour, A. R. & Sadeghi-Aliabadi, H. Sustainable synthesis of potential antitumor new derivatives of Abemaciclib and Fedratinib via CN cross coupling reactions using Pd/Cu-free Co-catalyst. *Mol. Catal.* **517**, 112011 (2022).
23. Aneeja, T., Neetha, M., Afsina, C. & Anilkumar, G. Progress and prospects in copper-catalyzed C-H functionalization. *RSC Adv.* **10**, 34429 (2020).
24. Boddapati, S. M. *et al.* Copper-promoted one-pot approach: Synthesis of benzimidazoles. *Molecules.* **25**, 1788 (2020).
25. Roy, T., Mahata, A. & Kundu, D. Recent advances in copper-catalyzed carbon chalcogenides cross-coupling reactions. *Curr. Org. Synth.* **20**, 267–277 (2023).
26. Wilson, K. A., Picinich, L. A. & Siamaki, A. R. Nickel–palladium bimetallic nanoparticles supported on multi-walled carbon nanotubes; versatile catalyst for Sonogashira cross-coupling reactions. *RSC Adv.* **13**, 7818–7827 (2023).
27. Varadwaj, G. B. B., Rana, S. & Parida, K. A stable amine functionalized montmorillonite supported Cu, Ni catalyst showing synergistic and co-operative effectiveness towards C–S coupling reactions. *RSC Adv.* **3**, 7570–7578 (2013).
28. Rimaz, S. *et al.* Insights into catalyst structure, kinetics and reaction mechanism during propane dehydrogenation on Pt–Ge bimetallic catalysts. *Appl. Catal. A Gen.* **643**, 118751. https://doi.org/10.1016/j.apcata.2022.118751 (2022).
29. Rai, R. K., Tyagi, D., Gupta, K. & Singh, S. K. Activated nanostructured bimetallic catalysts for C–C coupling reactions: Recent progress. *Catal. Sci. Technol.* **6**, 3341–3361 (2016).
30. Folsom, S. K., Ivey, D. J., McNair, F. S. & Siamaki, A. R. Nickel–Fe_3O_4 magnetic nanoparticles supported on multiwalled carbon nanotubes: Effective catalyst in Suzuki cross coupling reactions. *Catalysts.* **11**, 495 (2021).
31. Nair, P. P., Philip, R. M. & Anilkumar, G. Nickel catalysts in Sonogashira coupling reactions. *Org. Biomol. Chem.* **19**, 4228–4242 (2021).
32. Lipshutz, B. H., Nihan, D. M., Vinogradova, E., Taft, B. R. & Bošković, ŽV. Copper+ nickel-in-charcoal (Cu–Ni/C): A bimetallic, heterogeneous catalyst for cross-couplings. *Org. Lett.* **10**, 4279–4282 (2008).
33. Nasresfahani, Z. & Kassaee, M. Z. Bimetallic Ni/Cu mesoporous silica nanoparticles as an efficient and reusable catalyst for the Sonogashira cross-coupling reactions. *J. Organomet. Chem.* **937**, 121703. https://doi.org/10.1016/j.jorganchem.2021.121703 (2021).
34. Fu, Z., Li, T., He, X., Liu, J. & Wu, Y. The recyclable cyclopalladated ferrocenylimine self-assembly catalytic film and investigation of its role in the mechanism of heterogeneous catalysis. *RSC Adv.* **4**, 26413–26420 (2014).
35. Sarker, M. Z., Rahman, M. M., Minami, H., Suzuki, T. & Ahmad, H. Amine functional silica–supported bimetallic Cu–Ni nanocatalyst and investigation of some typical reductions of aromatic nitro-substituents. *Colloid Polym. Sci.* **300**, 279–296 (2022).
36. Ren, R., Li, T., Liu, M. & Wu, Y. Fabrication and catalytic properties of "cage like" aryl imine Pd(II)/Cu(II)-bimetallic catalytic monolayer supported on graphene oxide for Suzuki coupling reaction. *Chem. Eng. Sci.* **253**, 117604 (2022).
37. Huang, P. *et al.* Schiff-based Pd(II)/Fe(III) bimetallic self-assembly monolayer–-preparation, structure, catalytic dynamic and synergistic. *Mol. Catal.* **469**, 75–86 (2019).
38. Mara, M. W. *et al.* Unveiling ultrafast dynamics in bridged bimetallic complexes using optical and X-ray transient absorption spectroscopies. *Chem. Sci.* **13**, 1715–1724 (2022).
39. Mills, A. W. *et al.* General design rules for bimetallic platinum(II) complexes. *J. Phys. Chem.* **125**, 9438–9449 (2021).
40. Thoke, M. B., Sun, G.-J., Borse, R. A., Lin, P. & Lin, S.-X. Unimolecular cooperative metallaphotocatalysis with conjugately bridged Ir–Ni complexes and its applications in organic coupling reactions. *Org. Chem. Front.* **9**, 1797–1807 (2022).
41. Hazari, A. S., Chandra, S., Kar, S. & Sarkar, B. Metal complexes of singly, doubly and triply linked porphyrins and corroles: An insight into the physicochemical properties. *Chem. Eur. J.* **28**, e202104550 (2022).
42. Stott, T. L. & Wolf, M. O. Electronic interactions in metallated polythiophenes: what can be learned from model complexes. *Coord. Chem. Rev.* **246**, 89–101. https://doi.org/10.1016/S0010-8545(03)00114-0 (2003).
43. Gao, H. *et al.* Electronic coupling and electron transfer between two Mo_2 units through meta-and para-phenylene bridges. *Chem. Eur. J.* **25**, 3930–3938 (2019).
44. Liu, K., Shi, W. & Cheng, P. The coordination chemistry of Zn(II), Cd(II) and Hg(II) complexes with 1, 2, 4-triazole derivatives. *Dalton Trans.* **40**, 8475–8490 (2011).
45. Li, N. *et al.* Boosting electrocatalytic CO_2 reduction with conjugated bimetallic Co/Zn polyphthalocyanine frameworks. *CCS Chem.* **5**, 1130–1143 (2023).
46. Fa, D., Yuan, J., Feng, G., Lei, S. & Hu, W. Regulating the synergistic effect in bimetallic two-dimensional polymer oxygen evolution reaction catalysts by adjusting the coupling strength between metal centers. *Angew. Chem. Int. Ed.* **135**, e202300532 (2023).
47. Hajipour, A. R., Kalantari Tarrari, M. & Jajarmi, S. Synthesis and characterization of 4-AMTT-Pd(II) complex over Fe_3O_4@ SiO_2 as supported nanocatalyst for Suzuki-Miyaura and Mizoroki-heck cross-coupling reactions in water. *Appl. Organomet. Chem.* **32**, e4171 (2018).
48. Sobhani, S., Nasseri, F. & Zarifi, F. Unique role of 2-hydroxyethylammonium acetate as an ionic liquid in the synthesis of Fe_3O_4 magnetic nanoparticles and preparation of pyridine derivatives in the presence of a new magnetically recyclable heterogeneous catalyst. *J. Iran. Chem. Soc. J.* **15**, 2721–2732 (2018).
49. Geldard, J. F. & Lions, F. The organic chemistry of a new weak field tridentate chelating agent. 3,5-di(2-pyridyl)-1,2,4-triazole. *J. Org. Chem.* **30**, 318–319. https://doi.org/10.1021/jo01012a522 (1965).
50. Niakan, M., Karimi, S., Masteri-Farahani, M. & Shekaari, H. An efficient, cost-effective, and magnetically recoverable copper catalyst for O-arylation of phenols with aryl halides in choline chloride-based deep eutectic solvents. *Colloids Surf. A Physicochem. Eng. Asp.* **620**, 126603 (2021).
51. Ghasemi-Ghahsareh, A., Safaei-Ghomi, J. & Oboudatian, H. S. Supported l-tryptophan on Fe_3O_4@SiO_2 as an efficient and magnetically separable catalyst for one-pot construction of spiro [indene-2, 2′-naphthalene]-4′-carbonitrile derivatives. *RSC Adv.* **12**, 1319–1330 (2022).
52. Wu, N. *et al.* Structural evolution and synthesis mechanism of ytterbium disilicate powders prepared by cocurrent chemical coprecipitation method. *Ceram. Int.* **48**, 11545–11554 (2022).

53. Nikoorazm, M., Noori, N., Tahmasbi, B. & Faryadi, S. A palladium complex immobilized onto mesoporous silica: A highly efficient and reusable catalytic system for carbon–carbon bond formation and anilines synthesis. *Transit. Met. Chem.* **42**, 469–481 (2017).
54. Fekri, L. Z. & Zadeh, L. H. Copper/dapsone cuvalented Fe_3O_4@SiO_2-propyl nanocomposite as a highly active and magnetically recoverable Lewis acid catalyst for the novel synthesis of bis-dapsone derived acridines. *J. Chin. Chem. Soc.* **68**, 1673–1685 (2021).
55. Yao, Y. *et al.* Fabrication of Fe_3O_4/SiO_2 core/shell nanoparticles attached to graphene oxide and its use as an adsorbent. *J. Colloid Interface Sci.* **379**, 20–26 (2012).
56. Yang, X. *et al.* Interface modulation of chiral PPy/Fe_3O_4 planar microhelixes to achieve electric/magnetic-coupling and wide-band microwave absorption. *Chem. Eng. J.* **430**, 132747 (2022).
57. Kazemnejadi, M. *et al.* Imidazolium chloride-Co(iii) complex immobilized on Fe_3O_4@SiO_2 as a highly active bifunctional nano-catalyst for the copper-, phosphine-, and base-free Heck and Sonogashira reactions. *Green Chem.* **21**, 1718–1734. https://doi.org/10.1039/C8GC03919D (2019).
58. Lesiak, B. *et al.* Surface study of Fe_3O_4 nanoparticles functionalized with biocompatible adsorbed molecules. *Front. Chem.* **7**, 642 (2019).
59. Zaman, M. M. *et al.* Eco-friendly synthesis of Fe_3O_4 nanoparticles based on natural stabilizers and their antibacterial applications. *ChemistrySelect.* **4**, 7824–7831 (2019).
60. Kazeminezhad, I. & Mosivand, S. Phase transition of electrooxidized Fe_3O_4 to γ and α-Fe_2O_3 nanoparticles using sintering treatment. *Acta Phys. Pol. A.* **125**, 1210–1214 (2014).
61. Bentiss, F. *et al.* Corrosion control of mild steel using 3,5-bis(4-methoxyphenyl)-4-amino-1,2,4-triazole in normal hydrochloric acid medium. *Corros. Sci.* **51**, 1628–1635. https://doi.org/10.1016/j.corsci.2009.04.009 (2009).
62. Bentiss, F. *et al.* Improvement of corrosion resistance of carbon steel in hydrochloric acid medium by 3, 6-bis (3-pyridyl) pyridazine. *Int. J. Electrochem. Sci.* **7**, 1699–1723 (2012).
63. Mohanty, A., Kumar, S. & Tiwari, S. Assessment of N-(4H–1, 2, 4-triazol-4-yl) octanamide as hydrochloric acid corrosion inhibitor for mild steel. *Mater. Today Commun.* **27**, 102439 (2021).
64. Outirite, M. *et al.* Ac impedance, X-ray photoelectron spectroscopy and density functional theory studies of 3, 5-bis (n-pyridyl)-1, 2, 4-oxadiazoles as efficient corrosion inhibitors for carbon steel surface in hydrochloric acid solution. *Electrochim. Acta.* **55**, 1670–1681 (2010).
65. Liu, G. *et al.* Understanding the hydrophobic mechanism of 3-hexyl-4-amino-1, 2, 4-triazole-5-thione to malachite by ToF-SIMS, XPS, FTIR, contact angle, zeta potential and micro-flotation. *Colloids Surf. A: Physicochem. Eng. Asp.* **503**, 34–42 (2016).
66. Liu, G. *et al.* In situ probing the self-assembly of 3-hexyl-4-amino-1, 2, 4-triazole-5-thione on chalcopyrite surfaces. *Colloids Surf. A: Physicochem. Eng. Asp.* **511**, 285–293 (2016).
67. Vinoba, M., Bhagiyalakshmi, M., Jeong, S. K., Nam, S. C. & Yoon, Y. Carbonic anhydrase immobilized on encapsulated magnetic nanoparticles for CO_2 sequestration. *Chem. Eur. J.* **18**, 12028–12034 (2012).
68. Pan, F. *et al.* A facile molecular aggregation of isoquinoline based g-C_3N_4 for high photocatalytic performance under visible light illumination. *Mater. Res. Bull.* **152**, 111865 (2022).
69. Wei, Z. *et al.* High-efficiency adsorption of phenanthrene by Fe_3O_4–SiO_2-dimethoxydiphenylsilane nanocomposite: Experimental and theoretical study. *J. Hazard. Mater.* **422**, 126948 (2022).
70. Wang, X. *et al.* Constructing NiCo/Fe_3O_4 heteroparticles within MOF-74 for efficient oxygen evolution reactions. *J. Am. Chem. Soc.* **140**, 15336–15341 (2018).
71. Shin, H., Xiao, H. & Goddard, W. A. III. In silico discovery of new dopants for Fe-doped Ni oxyhydroxide ($Ni_{1-x}Fe_xOOH$) catalysts for oxygen evolution reaction. *J. Am. Chem. Soc.* **140**, 6745–6748 (2018).
72. Sultana, S. *et al.* Green synthesis of graphene oxide (GO)-anchored Pd/Cu bimetallic nanoparticles using Ocimum sanctum as bio-reductant: An efficient heterogeneous catalyst for the Sonogashira cross-coupling reaction. *RSC Adv.* **10**, 23108–23120 (2020).
73. Ghasemzadeh, M. S. & Akhlaghinia, B. FMMWCNTs@ CPA@ SMTU@ PdII NPs: As a versatile ferromagnetic nanostructured catalyst for Sonogashira-Hagihara cross-coupling reaction in solvent-Free conditions. *ChemistrySelect* **4**, 1542–1555 (2019).
74. Magdesieva, T. V., Nikitin, O. M., Yakimansky, A. V., Goikhman, M. Y. & Podeshvo, I. V. New heterobimetallic Cu(I)–Pd(II)-containing polymer complexes: Electrochemical synthesis and application in catalysis. *Electrochim. Acta.* **56**, 3666–3672 (2011).
75. Gholinejad, M. *et al.* Graphene quantum dots modified Fe_3O_4 nanoparticles supported PdCu with enhanced catalytic activity for Sonogashira reaction. *ChemCatChem.* **8**, 1442–1449 (2017).
76. Fan, X., Lin, D., Xu, Z. & Li, Y. Pd/Cu bimetallic catalyst immobilized on PEI capped cellulose-polyamidoamine dendrimer: Synthesis, characterization, and application in Sonogashira reactions for the synthesis of alkynes and benzofurans. *Colloids Surf. A Physicochem. Eng. Asp.* **648**, 129206 (2022).
77. Wang, G. *et al.* Copper and palladium bimetallic sub-nanoparticles were stabilized on modified polyaniline materials as an efficient catalyst to promote C–C coupling reactions in aqueous solution. *Nanoscales* **14**, 2256–2265 (2022).
78. Nasseri, M. A., Rezazadeh, Z., Kazemnejadi, M. & Allahresani, A. A Co–Cu bimetallic magnetic nanocatalyst with synergistic and bifunctional performance for the base-free Suzuki, Sonogashira, and C–N cross-coupling reactions in water. *Dalton Trans.* **49**, 10645–10660 (2020).
79. Martinez, E. E., Moreno, M. R., Barksdale, C. A. & Michaelis, D. J. Effect of precatalyst oxidation state in C–N cross-couplings with 2-phosphinoimidazole-derived bimetallic Pd(I) and Pd(II) complexes. *Organometallics* **40**, 2763–2767 (2021).
80. Pye, D. R. & Mankad, N. P. Bimetallic catalysis for C–C and C–X coupling reactions. *Chem. Sci.* **8**, 1705–1718 (2017).
81. Sharma, N. *et al.* Modified graphene supported Ag–Cu NPs with enhanced bimetallic synergistic effect in oxidation and Chan-Lam coupling reactions. *RSC Adv.* **10**, 30048–30061 (2020).
82. More, G. S., Kar, A. K. & Srivastava, R. Cu–Ce bimetallic metal–organic framework-derived, oxygen vacancy-boosted visible light-active Cu_2O–CeO_2/C heterojunction: An efficient photocatalyst for the Sonogashira coupling reaction. *Inorg. Chem.* **61**, 19010–19021 (2022).
83. Wang, C. *et al.* Mechanistic study of Cu–Ni bimetallic catalysts supported by graphene derivatives for hydrogenation of CO_2 to methanol. *J. CO2 Util.* **49**, 101542 (2021).
84. Giri, R. *et al.* Mechanism of the Ullmann biaryl ether synthesis catalyzed by complexes of anionic ligands: Evidence for the reaction of iodoarenes with ligated anionic CuI intermediates. *J. Am. Chem. Soc.* **140**, 793–806 (2018).
85. Huang, P. *et al.* Schiff-based Pd(II)/Fe(III) bimetallic self-assembly monolayer-preparation, structure, catalytic dynamic and synergistic. *Mol. Catal.* **469**, 75–86 (2019).
86. Gebresillase, M. N., Raguindin, R. Q., Kim, H. & Seo, J. G. Supported bimetallic catalysts for the solvent-free hydrogenation of levulinic acid to γ-valerolactone: Effect of metal combination (Ni–Cu, Ni–Co, Cu–Co). *Catalysts.* **10**, 1354 (2020).

Acknowledgements

The authors gratefully acknowledge the financial support by the Research Council of Tarbiat Modares University and University of Birjand.

Author contributions

F.N.: Writing—original draft, review & editing. M.A.N.: Supervision, review & editing. M.Z.K.: Supervision, review & editing. I.Y.: Supervision, review & editing.

Competing interests

The authors declare no competing interests.

Additional information

Supplementary Information The online version contains supplementary material available at https://doi.org/10.1038/s41598-023-44168-6.

Correspondence and requests for materials should be addressed to M.A.N.

Reprints and permissions information is available at www.nature.com/reprints.

Publisher's note Springer Nature remains neutral with regard to jurisdictional claims in published maps and institutional affiliations.